PROCEEDINGS OF
THE 2ND INTERNATIONAL WORKSHOP ON

COMPLEX PHYSICAL PHENOMENA IN MATERIALS

Hotel Armação, Porto de Galinhas - PE, Brazil
January 31- February 3, 2012

EDITED BY

Jon Otto Fossum and Giovani L. Vasconcelos

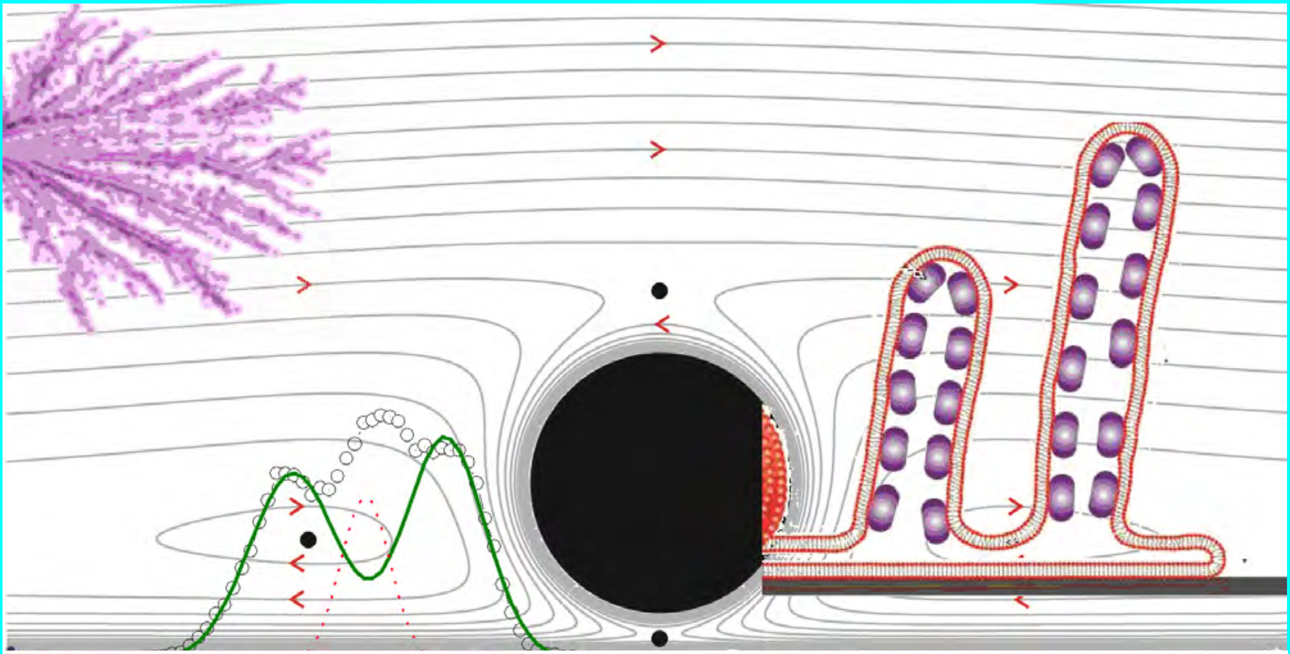

Universidade Federal de Pernambuco
DEPARTAMENTO DE FÍSICA

CAS OSLO

complex
www.complexphysics.org
Centre for Advanced Study
at the Norwegian Academy of Science and Letters

complexphysics.org
ISBN 978-82-93224-07-5

Proceedings of
2nd International Workshop on

Complex Physical Phenomena in Materials

Hotel Armação, Porto de Galinhas - PE, Brazil,
January 31- February 3, 2012

Edited by
Jon Otto Fossum and Giovani L. Vasconcelos

Webedition

Foreword

This book contains the proceedings from the 2nd International Workshop on "Complex Physical Phenomena in Materials," held at Hotel Armação, Porto de Galinhas, PE, Brazil, from January 31 to February 03, 2012.

The 1st Workshop, held in Recife, Brazil, from December 14-17, 2010, served as a venue for discussions on a wide range of complex phenomena in materials. The success of the 1st Workshop was a clear evidence of the importance of having meetings that promote interaction between scientists from different fields and from different working environments (universities, research institutes, and industry research centers). The 2nd Workshop followed these same guiding principles, as is evidenced by the contributions collected in these proceedings which represent a cross section of the research presented at the workshop.

The contributions presented in these proceedings are all related to presentations given at the workshop, and they have all been reviewed and accepted for publication in a process according to standard procedures with independent international referees.

The 2nd Workshop was made possible because of funds from the Brazilian agencies CAPES, FACEPE, and CNPq, and from the Research Council of Norway (RCN) through the RCN BILAT Program, and the Centre for Advanced Studies (CAS) of the Norwegian Academy of Sciences and Letters in Oslo, Norway. This meeting was part of a series of workshops organized by the Norwegian COMPLEX network project at CAS in 2011-2012, which included a workshop held in Hardanger, Norway, in August 2011, a workshop held in Havana, Cuba, in March 2012, and finally a workshop held in Svolvær, Norway, in May 2012, (see: www.cas.uio.no/research/1112complexmatter).

Finally, we would like to express our gratitude to our sponsors as well as to all the participants for their scientific contributions that made the workshop an enjoyable and successful meeting. We would also like to thank the Physics Department and the Physics Graduate Program at the Federal University of Pernambuco (UFPE), Recife, Brazil, for their support.

Jon Otto Fossum (NTNU, Norway) and *Giovani L. Vasconcelos* (UFPE, Brazil)

Editors

2nd International Workshop on Complex Physical Phenomena in Materials
Hotel Armação, Porto de Galinhas - PE, Brazil, January 31- February 3, 2012

Organized by

- Department of Physics and Graduate Program in Physics, Federal University of Pernambuco (UFPE), Recife, Brazil.
- Centre for Advanced Studies (CAS) of the Norwegian Academy of Sciences and Letters, Oslo, Norway.

Scientific committee:
Jon Otto Fossum (CAS – Oslo / NTNU-Trondheim, Norway), coordinator.
Giovani Lopes Vasconcelos (UFPE, Recife, Brazil)
Tom Henning Johansen (CAS – Oslo / University of Oslo, Norway).
Maurício Domingues Coutinho Filho (UFPE, Recife, Brazil)

Local organizing committee:
Giovani Lopes Vaconcelos (DF/UFPE), coordinator.
Ricardo Emmanuel de Souza (DF/UFPE)
Wilson Barros Jr. (DF/UFPE)

Finacial support:

- Coordenação de Aperfeiçoamento de Pessoal de Nível Superior (CAPES) - Brazil.
- Fundação de Amparo à Ciência e Tecnologia do Estado de Pernambuco (FACEPE) - Brazil.
- Conselho Nacional de Desenvolvimento Científico e Tecnológico (CNPq) - Brazil.
- Research Council of Norway (RCN) – Norway.

Contents

Participants at the 2nd International Workshop on "Complex Physical Phenomena in Materials," held at Hotel Armação, Porto de Galinhas, PE, Brazil, Jan. 31 – Feb. 3, 2012:

Brazil (32):
J. Albino Aguiar (UFPE, Recife)
José Andrade Jr. (UFC, Fortaleza)
Sérgio Campello (UFPE, Recife)
Marcio Carvalho (Pontificia Universidade Catolica do Rio de Janeiro, PUC-Rio)
Roosevelt Droppa Jr. (UFABC, São Paulo)
Miguel A. Durán (Instituto Federal do Sertão Pernambucano, Ouricuri, PE)
Mario Engelsberg (UFPE, Recife)
Daniel Espinosa (USP, São Paulo)
Rogelma Ferreira (UFC, Fortaleza)
Antonio M. Figueiredo Neto (USP, São Paulo)
Vanessa Janiszewski (UFPE, Recife)
Paulo N. Lisboa Filho (UNESP, Bauru)
André Galembeck (CETENE/UFPE, Recife)
Wilson Grava (CENPES, Petrobras, Rio de Janeiro)
Giovanni Grassi (UnB, Brasilia)
Leander E. Michels (UnB, Brasilia)
André Moreira (UFC, Fortaleza).
Maycon Motta (UFScar, São Carlos)
Marcel N. Moura (UFPE, Recife)
Fernando Oliveira (UnB, Brasilia)
Wilson Ortiz (UFScar, São Carlos, SP)
Hygor Piaget (UFC, Fortaleza)
Saulo D. S. Reis (UFC, Fortaleza)
J. Fernando Q. Rey (UFABC, São Paulo)
Sergio Rezende (UFPE, Recife)
Domingos Salazar (UFRPE, Recife)
Marcus B. L. Santos (UnB, Brasilia)
Matheus Sarmento (UFPE, Recife)
Adriaan Schakel (UFPE, Recife)
Antônio M. P. Silva (UFPE, Recife)
Geraldo José da Silva (UnB, Brasilia)
Giovani Vasconcelos (UFPE - Recife)

Argentina (1):
Diego M. Campana (Universidad Nacional del Litoral, CONICET, Santa Fe)

Cuba (1):
Ernesto Altshuler (Univ. Havana / CAS-Oslo, Norway)

France (3):
Françoise Brochard-Wyart (Institute Curie, Paris)
Paul Dommersnes (Univ. Paris 7 / CAS-Oslo, Norway)
Yves Meheust (Univ. Rennes 1, Geosciences /CAS-Oslo, Norway)

Norway (9):
Jon Alm Eriksen (Univ. Oslo)
Jon Otto Fossum (NTNU-Trondheim / CAS-Oslo)
Erling Fjær (SINTEF – Brasil, Rio de Janeiro)
Henrik Hemmen (NTNU, Trondheim)
Tom Henning Johansen (Univ. Oslo / CAS-Oslo)
Henrik Mauroy (IFE, Kjeller)
Arne Skjeltorp (IFE, Kjeller / CAS-Oslo)
Pawel Sobas (IFE, Kjeller)
Jørn Inge Vestgården (Univ. Oslo)

Sweden (1):
Irep Gözen (Univ. Chalmers, Gothenburg)

Switzerland (2):
Nuno Araújo (ETH Zurich)
Hans Herrmann (ETH Zurich)

USA (4):
Pablo Damasceno (Univ. Michigan)
Roger Pynn (Univ. Indiana)
Dan Rothman (MIT, Cambridge, MA)
Mark Mineev-Weinstein (NMC, Los Alamos)

Effect of surface roughness and surface defect density on the vortex configuration in a mesoscopic superconducting disk

J. Barba-Ortega[a], Edson Sardella[b], E.H. Brandt[c,*]and, J. Albino Aguiar[d,&]

[a] Grupo de Física Mesoscópica, Departamento de Física, Universidad Nacional de Colombia, Bogotá, Colombia, [b] UNESP-Universidade Estadual Paulista, Departamento de Física, Faculdade de Ciências, Caixa Postal 473, Bauru-SP, Brazil, [c] Max-Planck-Insitut für Metallforschung, D-70506 Stuttgart, Germany, [d] Departamento de Física, Universidade Federal de Pernambuco, 50670-901 Recife-PE, Brazil

* In memorian. [&] Contact e-mail: albino@df.ufpe.br

In this paper we study the superconducting properties of a flat disk by taking into account both the surface roughness and the influence of superficial defects. The sample is surrounded by a thin layer of a metallic material and submitted to and external magnetic field applied perpendicular to its plane. The boundary condition is taking into account via the de Gennes extrapolation length b. We evaluate the magnetization as a function of the external magnetic field, b parameter and rugosity. We show that the magnetic response is substantially modified by rugosity of the disk surface and that the competition between the confinement geometry and the geometric position of the defects leads to vortex configurations which are not compatible with the symmetry of the sample geometry.

Introduction

The study of the vortex matter in mesoscopic superconductors has been subject of great interest, particularly because of the resemblance with the atomic matter. This is a result of the interplay between vortex–vortex repulsion and the confinement produced by the external magnetic field induced screening currents. For finite size samples the vortices are formed at the surface and then pulled to the sample center by the Meissner shielding currents. But at the same time, a vortex is attracted to the sample edge which is described as the attraction to a virtual anti-vortex placed outside the sample. These competing interactions give rise to an energy barrier, the so-called Bean-Livingston surface barrier [1–2]. Surface roughness or defects in the interface may cause the local destruction of the surface barrier when a vortex enters a superconductor. Vortex configurations have been studied in superconducting slabs, square and rectangles [3-6] by using either the Ginzburg–Landau theory [3–5] or the London approach [6]. In several works the effect of the de Gennes boundary conditions on magnetization and vortex state for a mesoscopic superconducting samples was studied [7–12]. In this paper we will study the effects of the surface roughness, surface defects and different boundary conditions in the formation of vortices and how they influence on the first vortex penetration field. Also, we show how the competition between the sample geometry and the geometric position of the defects influence the vortex properties. We show that at low applied magnetic fields the vortex defect attraction dominates whereas at high applied magnetic field the vortex boundary repulsion is more important. This paper is organized as follows. First of all, we present the theoretical formalism which was used in order to find the magnetization, free energy and vortex configuration. Secondly, we present the results and discussions simultaneously. And finally, we present some conclusions.

Theoretical Formalism

The time dependent Ginzburg-Landau equations (TDGL) [2] which govern the superconductivity order parameter Ψ and the vector potential $\boldsymbol{A}$ in the zero electric potential gauge are given by:

$$\frac{\partial\Psi}{\partial t} = -\frac{1}{\eta}((-i\nabla - \mathbf{A})^2\Psi + (1-T)(|\Psi|^2 - 1)\Psi) \qquad (1)$$

$$\frac{\partial\mathbf{A}}{\partial t} = (1-T)\,\mathrm{Re}(\Psi^*(-i\nabla - \mathbf{A})\Psi) - \kappa^2\nabla\times\nabla\times\mathbf{A} \qquad (2)$$

Equations (1) and (2) were rescaled as follows: the order parameter Ψ in units of $\Psi_\infty(T)=(\alpha/\beta)^{1/2}$, where α and β are two phenomenological parameters. Temperatures in units of the critical temperature T_c, lengths in units of the coherence length $\xi(T)$, time in units of $t_0=\pi\hbar/96K_BT_c$, $\boldsymbol{A}$ in units of $Hc_2(T)T_c(T)$, where $Hc_2(T)$ is the second thermodynamics critical field. The Gibbs free energy in units of $G_0=(\alpha T_c)^2/\beta$. The dynamical equations are complemented with the appropriate boundary conditions for the order parameter. The general boundary condition for superconductors, found by de Gennes [2], is given by

$$\hat{n}.\left[-i\hbar\nabla + \frac{e^*}{c}\mathbf{A}\right]\Psi = \frac{-i\hbar}{b}\Psi$$

where $\hat{n}$ is the unity vector, perpendicular to the superconductor surface; b is the extrapolation de Gennes parameter. For all simulations we used $b > 0$, which describes the superconductor/metal interface. The full discretization of the TDGL equations can be found in more detail in Ref. [13,14]. We use the $U\Psi$ method to solve the TDGL equations in a discrete grid. Complex link variables U^x and U^y are introduced to preserve the gauge-invariant properties of the discretized equations [14].

Results

In Fig. 1 we illustrate the top surface of the disk which was generated randomly for a disk with a radius of R = 5.0 ξ(T), surface roughness of 15% and 20% and de Gennes extrapolation length b = ∞. In Fig. 2 (Left) we present the magnetization as a function of the external magnetic field H_0 for a disk of radius of R = 5.0 ξ (T), top surface with 10% roughness and several values of b (b = 0.83, 1.25, 2.5 and infinity). These curves present a typical profile of a magnetization curve of a mesoscopic superconductor [15,16]. It exhibits a series of discontinuities, in which each jump signals the entrance of one or more vortices into the sample. Notice that the number of jumps and the second thermodynamic field $Hc_2(T)$ varies significantly with b. The smaller the b value, less number of transitions we have.

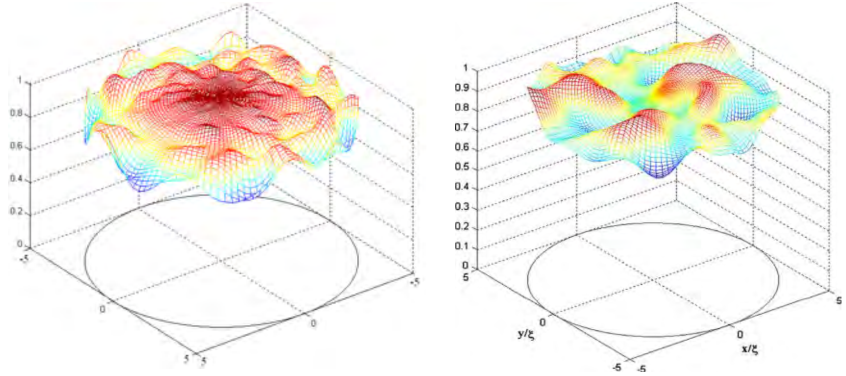

Figure 1
Examples of randomly generated surfaces which were used in the simulations for the 15% (left) and 20% (right) roughness, for a disk radius of R=5.0ξ(T) and for de Gennes extrapolation length $b = \infty$

Notice also that the third upper critical field $Hc_3(T)$, the field sufficient to destroy superconductivity, becomes smaller with decreasing b. On the other hand, b larger decreases the shielding capacity for the first penetration of vortices since the first penetration field becomes smaller as b increases. In Fig.2 (Right) we present the applied magnetic field dependence of the magnetization for the 0%, 5%, 10%, 15%, 20% roughness and $b = \infty$, for a disk of radius R = 5,0 ξ(T). For rugosity less than 5% the M vs H curves (not shown) resembles approximately the 5% rugosity curve. The rugosity has minor effect on the field corresponding to the transitions (the jumps in Figure 2 (Right)). As we can see from this figure, these fields are very close to one each other for all different values of the rugosity, except perhaps for 5%. In addition, they are very regular.

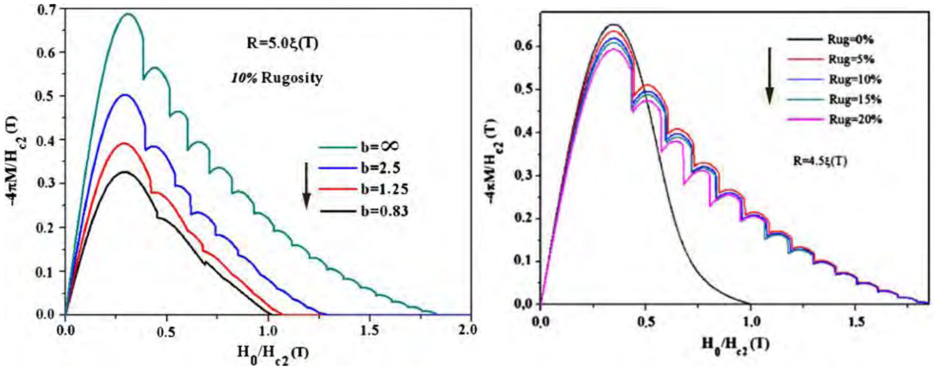

Figure 2

(Left) Magnetization curve as a function of the external applied magnetic field H_0 for different values of the de Gennes extrapolation length b = 0.83, 1.25, 2.5 and infinity. The others parameter are indicated inside the panel. (Right) Applied magnetic field H_0 dependence of the magnetization for $b = \infty$ and distinct values of the rugosity.

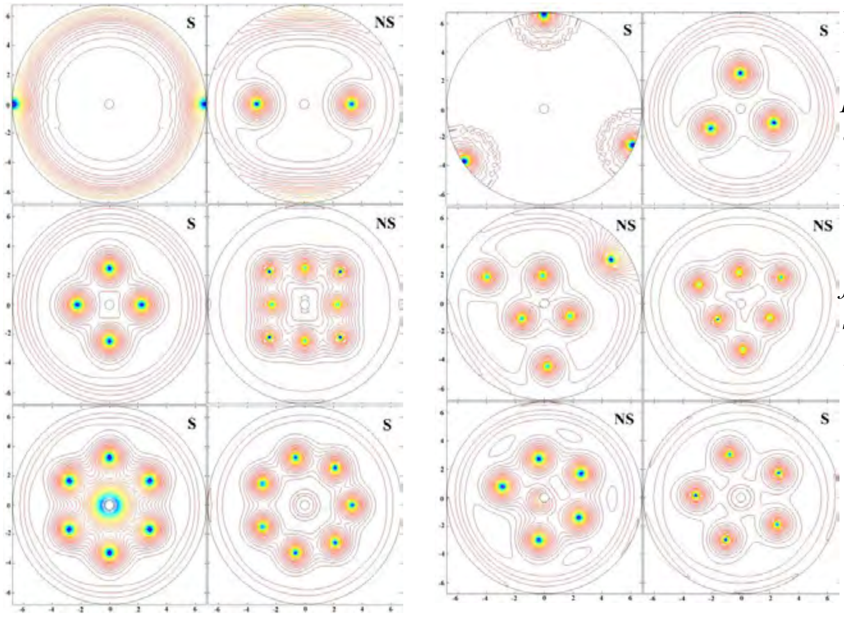

Figure 3

Contour plots of the order parameter for 2 and 3 defects placed symmetrically in the disk border, for a disk with a radius R = 6.5 ξ(T). The symbols S and NS stand for stationary and non-stationary configurations, respectively.

In Fig. 3 we show the contour plot of the order parameter for several vorticities, for two (three) defects positioned symmetric with respect to the center of the disk, for a flat disk of radius R = 6.5 ξ(T). Following the panels from the left to the right and from the top to the bottom, in this order, we can see that initially two (three) vortices are trying to nucleate at the defect positions. At a certain external applied field two (three) vortices are formed and move to the center horizontally. At this same field another two (three) vortices enter and the four (six) vortices will set into a square (triangle). As the applied external field is increased, four (one) more vortices will be formed and they try to accommodate into a square (pentagon). However, these are not stables configurations. Although the energy of this metastable state is very close to the stationary state, the vortices will rapidly move and arrange into a configuration of two vortices at the center (making a giant vortex) and the six (five) other vortices will be distributed around it in a circular arrangement; the absolute difference in energy between the two configurations is of the order 10^{-6}. If the strength of the surface defects are increased this square (triangle) configuration can become a stable configuration. In fact, there is a competition between the symmetry imposed by the defects and the geometry of the superconducting sample. When further increasing the field we found a circular chain of seven (five) vortices with equal distance from the center and a single vortex at the center.

Conclusions

We performed a study of vortex configurations and the magnetic properties in thin superconducting disk submitted to a homogeneous external magnetic field. We calculated the magnetization and critical magnetic fields numerically by solving the TDGL equations. We have shown that the magnetization curve is substantially modified by taking into account the surface rugosity of disk and also by considering a surrounding which can be either a metal or an insulator. Also, we obtained the stable, metastable and transient vortex configurations in a thin superconducting disk with different number of surface defects. The competition between the symmetry imposed by the defects and the geometry of the superconductor results in different non-conventional vortex configuration. At low magnetic field the position of the defects determine mainly the vortex configuration while for high magnetic field it is the geometry of the superconducting sample that determines the vortex configuration.

Acknowledgments

This work was financed by the Brazilian Agencies CAPES, CNPq and FACEPE (APQ-0589/1.05-08) and Colombian Agencies, DIB, COLCIENCIAS (RC 696).

References

[1] C. P. Bean, J. D. Linvsgton, Phys. Rev. Lett. 12, 14 (1964)
[2] P. G. de Gennes, Superconductivity in Metals and Alloys (Addison-Wesley, Reading, MA, 1989).
[3] A.A. Abrikosov, Soviet Phys. JETP 5, 1174 (1957)
[4] A.A. Abrikosov, Phys. Chem. Solids 2, 199 (1957)
[5] E.H. Brandt, Rep. Prog. Phys. 58, 1465 (1995)
[6] V.R. Misko, V.M. Fomin, J.T. Devreese, V.V. Moshchalkov, Phys. Rev. Lett. 90, 147003 (2003)
[7] V. Oboznov, I.V. Grigorieva, Europhys. Lett. 83 (2008) 17008 (2008)
[8] L.R.E. Cabral, B.J. Baelus, F.M. Peeters, Phys. Rev. B 70. 144523 (2004)
[9] J. Barba-Ortega, E. Sardella, J.Albino Aguiar, Supercond. Sci. Technol. 24, 015001 (2011)
[10] E. Sardella, E.H. Brandt, Supercond. Sci. Technol. 23, 025015 (2010);
E. Sardella, P.N. Lisboa-Filho, A.L. Malvezzi, Phys. Rev. B 77, 104508 (2008)
[11] J. Barba-Ortega, Edson Sardella, J. Albino Aguiar, Physica C 470, 1964 (2010)
[12] J.J. Barba, L.R.E. Cabral, J. Albino Aguiar, Physica C 460, 1272 (2007)
[13] J. Barba-Ortega, E. Sardella, J. Albino Aguiar, Supercond. Sci. Technol. 23, 2415001 (2011)
[14]E. Sardella, P.N. Lisboa-Filho, A.L. Malvezzi, Phys. Rev. B 77, 104508 (2008)
[15] B. J. Baelus, K. Kadowaki, and F. M. Peeters, Phys. Rev. B 71, 024514 (2005)
[16] I. V. Grigorieva, W. Escoffier, V. R. Misko, B. J. Baelus, F. M. Peeters, L. Y. Vinnikov, and S. V. Dubonos, Phys. Rev. Lett. 99, 147003 (2007)

Numerical computations under visco-inertial regime of the dip coating on fibers

D. M. Campana[1,2], S. Ubal[1,2], M. D. Giavedoni[2] and F. A. Saita[2]

[1] INTEC, Universidad Nacional del Litoral – Conicet, Güemes 3450, 3000 Santa Fe, Argentina, [2] Facultad de Ingeniería, Universidad Nacional de Entre Ríos, Ruta 11, Km. 10, C.C. 47 – Suc. 3-3100 Paraná, Argentina.

Contact email: dcampana@santafe-conicet.gov.ar

The dip coating of a fiber of small radius is studied via a finite element solution of the Navier-Stokes equations. The coating speed is selected within the range corresponding to the visco-capillary regime and the visco-inertial regime. Predictions obtained for the visco-capillary regime are in very good agreement with the Landau-Levich law as well as with published experiments; while those obtained for the visco-inertial regime —i.e. at coating speeds typical of industrial applications— agree well with published experimental data.

Introduction

Dip coating is a method used to deposit a thin uniform film on a solid by withdrawing it at a constant speed from a bath containing the liquid to be coated (see Figure 1). It has been one of the most extensively studied coating processes since the pioneering work carried out by Landau and Levich [1], who developed an approximate expression for the film thickness valid at very low withdrawal speeds and when the effects of gravity are negligible (visco-capillary regime). In industrial applications, however, the withdrawal velocity is frequently very high (tens of m/s), inertia being a dominant force on the system mainly in the dynamic menisci where the film is formed (visco-inertial regime). Experimental works show that there is a limiting velocity from which the film thickness and the size of the meniscus grow abruptly [2, 3]. Numerical solutions of the full hydrodynamic problem when the substrate is a plate include the effects of inertia [4], and soluble [5] and insoluble surfactants [6] on the film thickness. However, it appears that to the authors' best knowledge, no attempt has been made to numerically study the case of fiber coating at large velocities; i. e., when the role of inertia cannot be neglected. Thus, one of the goals of this work is to predict the film thickness formed on a cylindrical fiber pulled out of a liquid by numerically solving the Navier-Stokes equations, within the range of the parameters corresponding to the visco-inertial regime of the experiments already mentioned.

The Model

A small cylindrical fiber of radius R is vertically pulled out of a large liquid bath at constant speed U. The liquid is Newtonian with viscosity μ and density ρ and the air above it is considered inviscid and its pressure is arbitrarily set equal to zero. The fiber contacts the liquid at a distance H below the free surface; the coating fluid is a pure liquid and the temperature of the system is uniform; therefore, the gas-liquid surface tension, σ, is constant. Therefore, this process taking place in the flow domain and coordinate system shown in Figure 1 is governed by the Navier-Sokes and continuity equations. In dimensionless form, these equations read,

$$\nabla \cdot \mathbf{v} = 0 \tag{1}$$

$$Re(\mathbf{v}\cdot\nabla\mathbf{v})=-\frac{1}{Ca}\nabla p+\nabla^2\mathbf{v}-\frac{Bo}{Ca}\mathbf{e}_z \qquad (2)$$

The characteristic scales used are U for velocities, R for lengths, R/U for time, and σ/R for pressures; in the above expressions, $Re=\rho RU/\mu$ is the Reynolds number, $Ca=\mu U/\sigma$ is the capillary number, and $Bo=\rho gR^2/\sigma$ is the Bond number that measures the ratio between gravity and capillary forces.

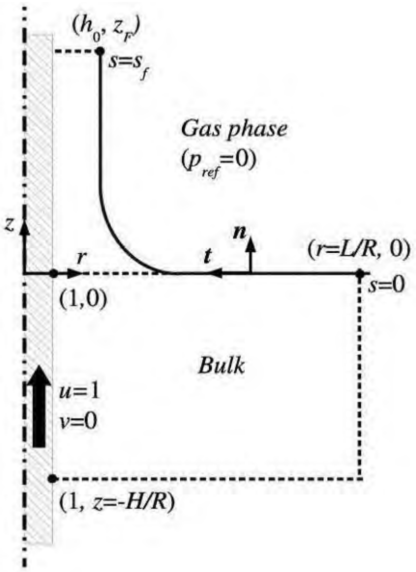

Figure 1
Sketch of the flow domain in dimensionless variables.

The boundary conditions imposed are as follows. On the surface of the fiber the non slip condition is imposed as Dirichlet conditions. The rest of boundary conditions, to be detailed below, was applied as Neumann boundary conditions by introducing the corresponding changes in the components of the stress tensor at each boundary. At the bottom boundary in $z=-H^*$, we impose no flow changes along the z coordinate and the pressure is assumed approximately hydrostatic. At the lateral boundary of the domain ($r=L^*$) far away from the fiber, we assume both the flow is in the radial direction only and that the pressure is mainly hydrostatic. At the film exit boundary ($z=z_F$), we assume that the flow is unidirectional and it does not change in the axial direction.

To establish the boundary conditions at the free surface we presume that the interface is a material surface; therefore, the kinematic condition applies

$$\mathbf{v}\cdot\mathbf{n}=0 \qquad (3)$$

The free surface is Newtonian, inviscid and since the system is free of surfactant, surface tension is constant and thus the interfacial balance of stresses results

$$\mathbf{n}\cdot\mathbf{T}=\frac{1}{Ca}\left[\frac{d\mathbf{t}}{ds}-\frac{(\mathbf{e}_r\cdot\mathbf{n})\mathbf{n}}{r_S}\right], \qquad (4)$$

where r_S is the local interfacial radius and **n** is the outwardly directed unit vector normal.

Numerical Technique

Details of the numerical technique will not be included here. We only mention that the system of governing equations and their boundary conditions were discretized by the finite elements method (Galerkin and mixed velocity-pressure formulation) and solved using the commercial finite element software COMSOL Multiphysics in a similar manner as described in [7]. We check the correctness of the solution by doing several test over the discretization and size of the domain and comparing the solution with theoretical and experimental results as it will be shown in the next section.

Results

a)

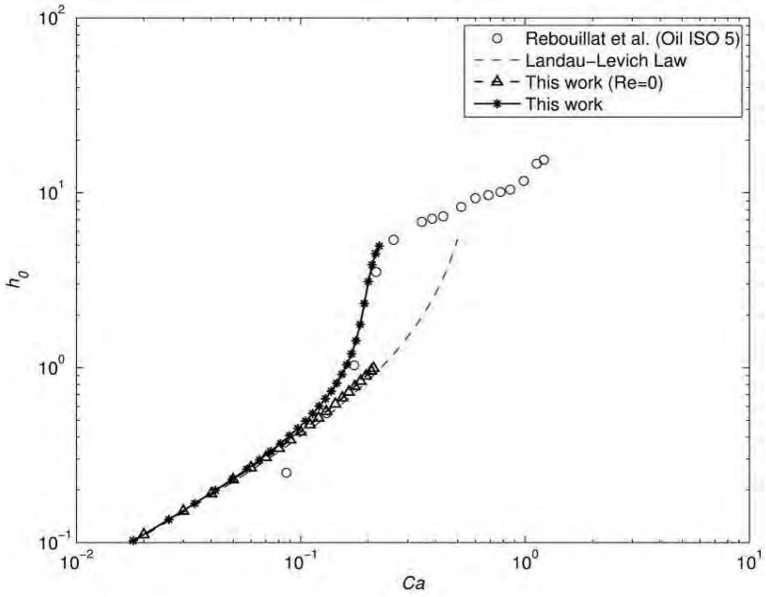

Figure 2

a) Comparison of the experimental film thickness (ISO 5) with the LLD law and results of the numerical code;

b)

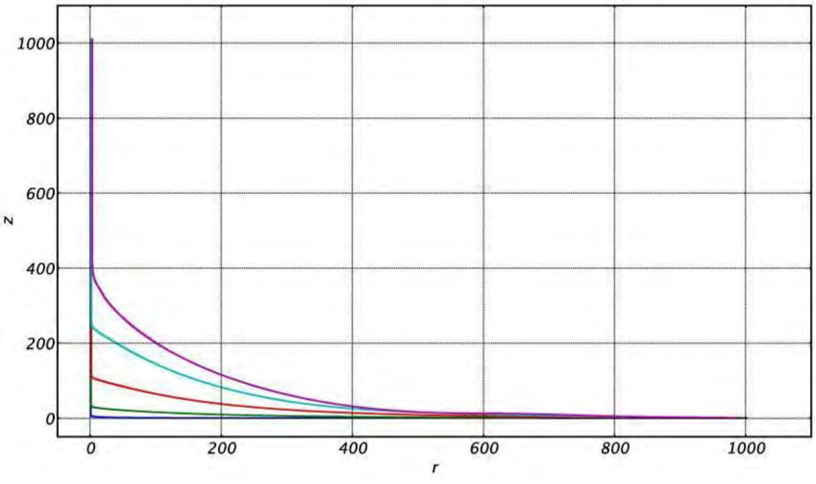

b) interfacial shapes at Ca = 0.01, 0.06, 0.11, 0.16 and 0.18.

When the fiber is small and the withdrawal velocity is low, the thickness of the liquid film can be determined by the LLD law, which gives the following expression for the non-dimensional thickness: $h_0 = 1.34Ca^{2/3}$. Figure 2(a) shows the excellent agreement between the results of our numerical code, for Re=0, and LLD law. However, experiments carried out by de Ryck and Quéré [2] and Rebouillat et al. [3] show that there exists a value of the Capillary number (Ca*) above which the film thickness sharply increase. The onset of this increase (Ca*) can be approximately determined by doing a balance between the inertial and surface tension forces in the problem, that is doing the Weber number equal to one. Rebouillat et al. use in their experiments an "oil 5" with the following properties $\mu=6.5\times10^{-3}$ Pa s, $\rho=822$ kg/m^3, and $\sigma = 2.46\times10^{-2}$ N/m, while the diameter of the fiber was equal to 54 μm. Thus, the balance gives $Ca^* \sim 0.27$, which is very close the experimental value observed in Figure 1(a). When the parameters in our code are set to reproduce this experimental condition, we get an excellent agreement as can be noted. Figure 2(b) depicts interfacial shapes at different velocities, they show notable interfacial deformations experienced by the meniscus; they are larger as the inertia becomes more important.

Conclusion

In this work a numerical solution of the dip coating of a fiber of small radius is presented. The model was validated by comparing its predictions with the LLD theory and it was used to reproduce reported results obtained from experiments carried out in the visco-inertial regime. In the region where the visco-inertial regime starts to prevail, our numerical predictions agree surprisingly well with the experimental values already published. These results show the ability of the numerical technique to give accurate predictions when non-linear effects are dominant.

Acknowledgements

We gratefully acknowledge ANPCyT, UNL, and CONICET for financially supporting this work.

References:

[1] Landau, L., and Levich, B. *Dragging of a liquid by a moving plate*. Acta Physicochimica URRS 17, 42-54 (1942)

[2] De Ryck, A., and Quéré, D. *Inertial coating of a fibre*. Journal of Fluid Mechanics 311, 219-237 (1996)

[3] Rebouillat, S., Steffenino, B., and Salvador, B. *Hydrodynamics of high-speed fibre impregnation: the fluid layer formation from the meniscus*. Chemical Enginnering Science 57, 3953-3966 (2002)

[4] Jin, B., Acrivos, A., and Münch, A. *The drag-out problem in film coating*, Physics of Fluids, 17 (103603),1-12 (2005)

[5] Campana, D.M., Ubal, S., Giavedoni, M.D., and Saita, F A. *Numerical prediction of the film thickening due to surfactants in the Landau-Levich problem*. Physics of Fluids, 22 (032103) 1-9 (2010)

[6] Campana, D.M., Ubal, S., Giavedoni, M.D., and Saita, F A. *A deeper insight into the dip coating process in the presence of insoluble surfactants: a numerical analysis.* Physics of Fluids, 23 (052102) 1-11 (2011)

[7] Ubal, S. Xu, B., Derby, B. And Grassia, P. *Continuous deposition of a liquid thread onto a moving substrate. Numerical analysis and comparison with experiments*, Journal of Fluid Engineering (ASME), in press.

Interface growth in a channel and tripolar Loewner evolutions

Miguel A. Durán[1] and Giovani L. Vasconcelos[2]

[1]Instituto Federal de Educação, Ciência e Tecnologia do Sertão Pernambucano – Ouricuri, PE, [2] Departamento de Física, Universidade Federal de Pernambuco, Recife, PE, Brazil.

Contact email: [1]miguel.duran@ifsertao.edu.br, [2]giovani@df.ufpe.br

Abstract:
The Loewner equation describes a rather general class of growth processes in two dimensions where a curve starts from a given point on the boundary of a certain "physical domain" in the complex z-plane and grows into the interior of this domain. The growth dynamics is then conveniently described in terms of a conformal mapping $g_t(z)$*, from the physical domain onto a suitable "mathematical domain", which satisfies a first-order ordinary differential equation—the so-called Loewner equation. In this work, a class of Laplacian growth models in a Hele-Shaw channel is studied using the formalism of tripolar Loewner evolutions, in which three points, namely, the channel corners and the point at infinity, are kept fixed. A model for interface growth is formulated in terms of a generalized tripolar Loewner equation and several examples are presented.*

The Loewner equation [1] describes a rather general class of growth processes in two dimensions where a curve starts from a given point on the boundary of a domain $\mathbf{P}$ in the complex z plane and grows into the interior of $\mathbf{P}$. More specifically, the Loewner equation [2] is a first-order differential equation for the conformal mapping $g_t(z)$, from the "physical domain," consisting of the region $\mathbf{P}$ minus the curve, onto a "mathematical domain" represented by $\mathbf{P}$ in an auxiliary complex w plane.

Here we consider the problem of Loewner evolutions in the so-called channel geometry [3,4], where the domain $\mathbf{P}$ consists of the upper half channel defined by: $-1 \leq x \leq 1, y > 0$. More specifically, we consider an interface starting from a segment, $[x_1, x_2]$ C $[-1,1]$, on the real axis in the z plane and growing into the upper half channel $\mathbf{P}$, as indicated in Fig. 1. In Ref. [4] we introduced a rather general class of growth models in this geometry where it was assumed, for simplicity, that the interface had certain special points, referred to as tips and troughs, where the growth rate is a local maximum and a local minimum, respectively, while the interface end points x_1 and x_2 remain fixed. In particular, it was shown [4] that in the long-time asymptotics the interface evolves into a steadily moving finger. In the present work we focus on the initial stages of the evolution. In the next paragraph we formulate the model, after which we derive the corresponding Loewner equation for the model, and then present some examples of interface evolutions.

Let us denote by Γ_t the interface at time t and by K_t the growing region delimited by Γ_t and the real axis. It is assumed that the curve Γ_t is simple, so that the physical domain, represented by the channel without the region K_t (i.e., $\mathbf{P}\backslash K_t$), is simply connected. The Loewner function $g_t(z)$ is defined by the following property: it maps the physical domain $\mathbf{P}\backslash K_t$ in the z plane onto the domain $\mathbf{P}$ itself in the mathematical w plane (i.e., $g_t : \mathbf{P}\backslash K_t \rightarrow \mathbf{P}$). Under the action of $g_t(z)$, the interface Γ_t is mapped to an interval $[[a]_1(t), a_2(t)]$ on the real axis in the w plane, with the end points x_1 and x_2 being mapped to the points $a_1(t)$ and $a_N(t)$, respectively, while the tips and troughs are mapped to points $a_i(t) \in]a_1(t), a_N(t)[$, for $i = 1, 2, \ldots, N-1$, where N is the total number of such special points, that is, the number of tips and troughs plus the two end points (see Fig. 1). The mapping function $g_t(z)$ is required to keep the channel corners fixed, i.e., $g_t(\pm 1) = \pm 1$. The point at infinity $z = i\infty$ is also kept fixed by $g_t(z)$, owing to the so-called hydrodynamic normalization: $g_t(z) \approx z$, for $z \to i\infty$; see [4] for a detailed discussion of the meaning of the hydrodynamic condition in the channel geometry. Because the Loewner mapping $g_t(z)$ fixes these three points, i.e., $z = \pm 1$ and $z = i\infty$, we refer to growth processes in the channel geometry as *tripolar* Loewner evolutions. In addition to the three boundary conditions above, the Loewner function must satisfy the initial condition $g_0(z) = 0$, since one starts with an empty channel. The growth dynamics in our model is specified by requiring that tips and troughs grow along gradient lines in such a way that the interface $\Gamma_{t+\tau}$, for infinitesimal τ, is mapped under $g_t(z)$ to a polygonal curve, as shown in Fig. 1.

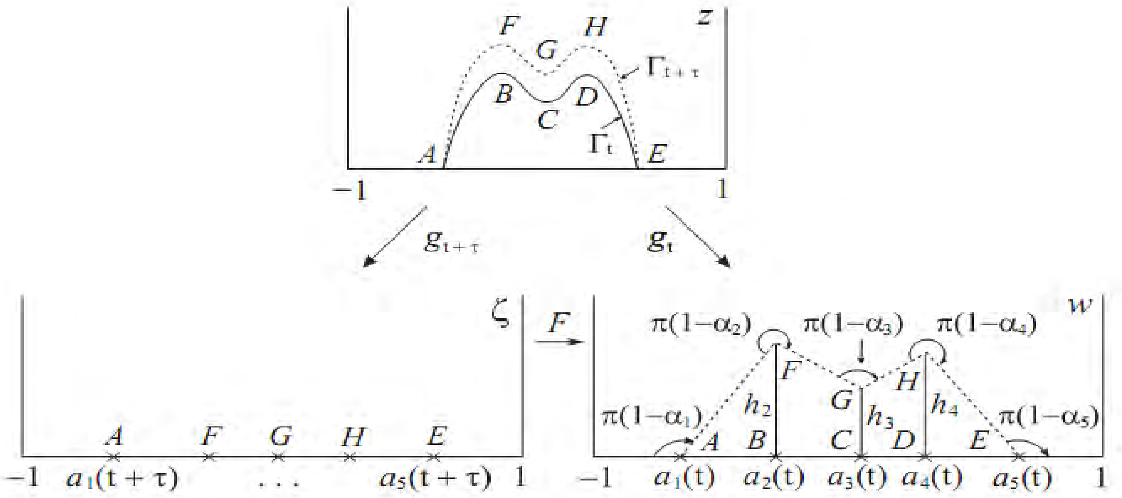

Figure 1
The physical and mathematical planes for a growing interface in the channel geometry. The mapping $g_t(z)$ *maps the interface* Γ_t *to a segment on the real axis, while the new interface* $\Gamma_{t+\tau}$ *is mapped to a polygonal curve.*

As described in detail in [4], it is convenient to use the transformation $\Phi(z) = \sin(\pi/2\ z)$ to map the upper half-channel onto the upper half-plane, where it becomes easier to derive the corresponding Loewner equation. After some straightforward calculation [4], one obtains the following tripolar Loewner equation in the upper half-plane:

$$\dot{g}_t(z) = A_-(t) - A_+(t) g(z) + \sum_{i=1}^{N} d_i(t) [g_t(z) - a_i(t)] ln[g_t(z) - a_i(t)] \qquad (1)$$

where

$$A_\pm(t) = \sum_{i=1}^{N} d_i(t) \{[1 + a_i(t)] ln[1 + a_i(t)] \pm [1 + a_i(t)] ln[1 + a_i(t)]\}$$

The time evolution of the driving functions $a_i(t)$ are determined by the following set of ordinary differential equations:

$$\dot{a}_i = A_-(t) - A_+(t)a_i(t) + \sum_{j=1}^{N} d_i(t)[a_i - a_j]\ln|a_i - a_j|, \qquad i = 1, \dots, N$$

The growth factors $d_i(t)$ control the growth rates of the tips and troughs [4], and for simplicity we shall assume that they are all constant, i.e., $d_i(t) = d_i$.

In what follows we will present several examples of interface evolutions obtained from the numerical integration of the Loewner equation (1). First, a symmetric interface is shown in Fig. 2, where the solid curves represent the interface at various times *t*. One sees from this figure that as time proceeds the interface quickly expands and tends to occupy the entire channel, so that for longer times $(t \to \infty)$ a steadily moving finger with width equal to the channel width results [4]. In Fig. 3 we show a solution for an asymmetric interface. As seen in this figure, the tip is initially "repelled" by its image with respect to the closest channel wall and for sufficiently long time an asymmetric finger (i.e., with the tip off center) will result. In Fig. 4 we show an example where the interface has two tips and one trough. In this case, the tip growth factors are different leading to "tip competition" (i.e., the left tip falls behind the other tip), so that for later times an asymmetric finger is expected to form.

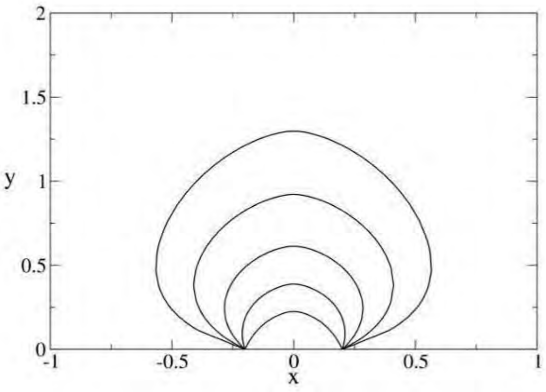

Figure 2
Loewner evolution for an interface growing from a segment on the channel base. The curves show the interface at different times.

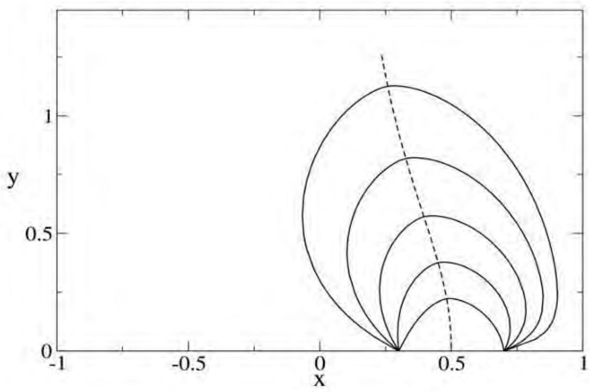

Figure 3
Loewner evolution for an asymmetric interface growing in the channel geometry. The dashed curve represents the path traced by the tip.

In Fig. 5 we show numerical solutions for two growing symmetrical interfaces, with one tip each. Here the interfaces start to grow from the intervals [-3,-1] and [1,3], respectively, with the corresponding tips starting at symmetrical points. Notice that as time goes by the inner sides of the two interfaces move towards one another leaving a narrow channel between them. For sufficiently large time, the width of such a channel becomes infinitesimally small so that for all practical purposes the resulting evolution will look like a single symmetrical finger. If the symmetry between the two interfaces is broken, then "finger competition" ensues and one finger will eventually move ahead of the other one, resulting in a single asymmetric finger in the asymptotic limit.

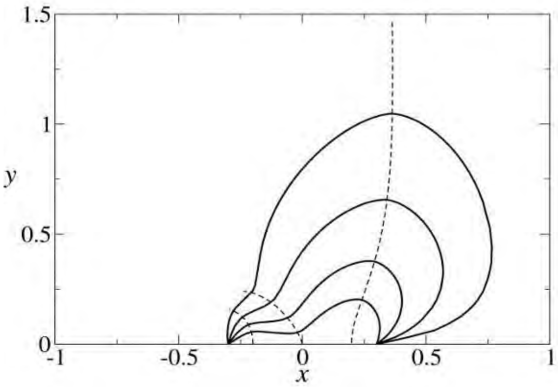

Figure 4
Asymmetrical growing interface with two tips in the channel. The dashed lines represent the trajectories of the tips and of the trough.

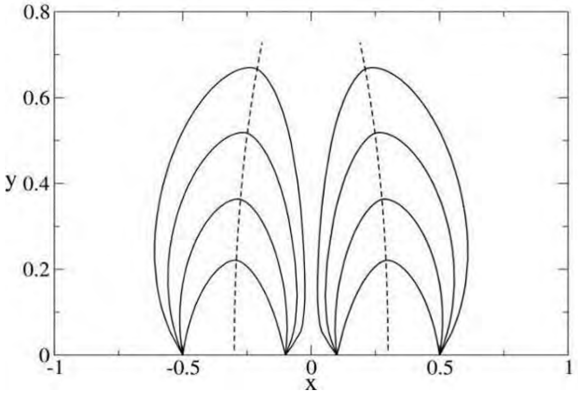

Figure 5
Loewner evolution for two symmetrical interfaces.

In conclusion, we have studied an interface growth model in the channel geometry in terms of tripolar Loewner evolutions. In particular, we have shown that if one starts with an asymmetric configuration (with either multiple tips or multiple interfaces) then there is competition among the tips in the early stages of the evolution, which leads to the formation of an asymmetric finger in the long-time asymptotic regime.

Acknowledgments

This work was supported in part by the Brazilian agencies CNPq and FACEPE.

References

[1] K. Loewner, Math. Ann. 89, 103 (1923).
[2] For reviews, see, e.g., I. A. Gruzberg and L. P. Kadanoff, J. Stat. Phys. 114, 1183 (2004); and M. Bauer and D. Bernard, Phys. Rep. 432, 115 (2006).
[3] T. Gubiec and P. Szymczak, Phys. Rev. E 77, 041602 (2008).
[4] Miguel A. Durán and Giovani L. Vasconcelos, Phys. Rev. E 84, 051602 (2011).

Roughness of Fractures in Laponite Gels determined by Magnetic Resonance Imaging

H. Hemmen,[1] E. N. de Azevedo,[2] M. Engelsberg,[3] and J.O. Fossum.[1,4]

[1]Department of Physics, NTNU, Trondheim, Norway, [2]Núcleo de Tecnologia - Centro Acadêmico do Agreste, UFPE, Caruaru, Brazil, [3]Departamento de Física, UFPE, Recife, Brazil, [4]2011-12: Centre for Advanced Study – CAS, at the Norwegian Academy of Science and Letters, Oslo, Norway

Contact email: henrik.hemmen@ntnu.no, jon.fossum@ntnu.no

Experimental determination of the roughness of fractures in gels is reported. The studied gel is prepared by dispersing the synthetic clay Laponite RD in de-ionized water. A novel way of finding the roughness exponent through the use of Magnetic Resonance Imaging is developed. By recording the ^1H *signal intensity from slices of the clay gel, the clay–air interface can be imaged. From the one dimensional height profiles obtained in this manner, the roughness exponent is calculated using standard methods found in the literature.*

We create fracture surfaces by a controlled removal of filter paper attached to the surface of the gel. By studying fracture surfaces created with Mode-I fracturing, the roughness exponent is found to be 0.56 (+0.05,-0.07), with no dependence between fracturing speed and roughness. On the other hand, using a combination of Mode-I and Mode-II fracturing, a velocity-dependent roughness in the direction perpendicular to the fracturing is revealed. A connection with the shear thinning behaviour of Laponite gels is proposed.

The growth and structure of rough interfaces is a field that has attracted considerable attention in recent years, see e.g. the review articles by Meakin [1], Bouchaud [2], and Persson et al. [3]. In order to search for universality in rough interfaces, experimental studies have been performed on a wide range of materials, such as wood, steel, plaster, porcelain, polymer gels, etc. However, most of these materials are brittle, and little work has been performed on fractures in soft matter. In this study, we investigate the roughness of fractures in Laponite gels.

Laponite is a synthetic 2:1 layered swelling clay consisting of disk-like platelets with approximate thickness 1 nm and average diameter close to 200 Å [4]. It has commercial application in a wide range of fields, including surface coatings and personal care products, as well as in the oil industry and agriculture. When dispersed in water, even at concentrations below 2%, the dispersion undergoes a liquid-solid transition, forming a clear transparent gel [5].

Characterization of fracture surfaces are mainly done by studying their fractal self-affinity: $(x,y,z) \rightarrow (\lambda x, \lambda y, \lambda^{\zeta} z)$, from which one can extract the roughness exponent ζ. The most common method of determining ζ is to measure one dimensional height profiles, and then use one of several methods to calculate ζ from correlations in the profiles. This is a challenge with Laponite gels, as their softness makes mechanical profilometry unsuitable, and their transparency means optical methods require the use of special dyes. In this work we take a novel approach, and use MRI to image slices of fractured Laponite gels. From the slices we can extract height profiles, and calculate the roughness exponent. This is to our knowledge the first time MRI has been used for roughness characterization, and also the first study of roughness in Laponite gel fractures.

The MRI images were obtained with an INOVA spectrometer manufactured by Varian Inc. The spectrometer includes a 2.0 T horizontal cryocooled superconducting small bore magnet made by Oxford Instruments, and an RF coil, manufactured by Varian Inc. (internal diameter 6 cm, length 16 cm). The operating frequency of the system is 85.007 MHz.

Laponite RD was purchased from Rockwood Additives Ltd, and the gels were prepared according to the recommendations by the manufacturer [6]: 3 w/w % Laponite powder was added to deionized water at room temperature. The water was stirred in a beaker using a magnetic stirrer until all visible aggregates had dissolved, and then for an additional 30 minutes. During the mixing, the solution evolves from a white opaque, to a transparent water-like liquid. Immediately after mixing, the Laponite–water solution was poured into $5\times5\times2.5\ \text{cm}^3$ ($w\times l\times h$) plastic sample holders. The samples were then placed in air-tight containers together with a small cup of water for at least 24 h, before they were studied.

The experimental method for making fracture surfaces was based upon the peel-test-like method employed by Tanaka et al. [7], as illustrated in Figure 1. A filter paper was attached to the top of the gel by pressing it gently onto the surface, and letting water enter the paper for about 20 minutes. When the filter paper was removed, an approximately 1 mm thick layer of Laponite stuck to the filter paper and a fracture surface was left behind. A stepping motor 1331T006S from Faulhaber was used to control the fracturing velocity, which was varied in the range 10-90 mm/min.

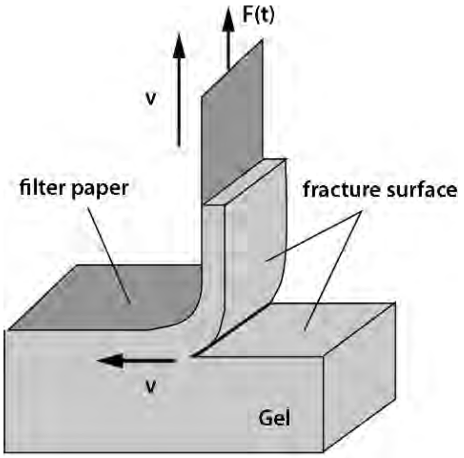

Figure 1
Fracturing the Laponite gel. Adapted from [7]

We used the MRI setup to record the spin density within slices of the sample. Each slice had a thickness of 0.23 mm, and the typical resolution within the slice was 0.23 mm × 0.12 mm, with the highest resolution perpendicular to the fracture plane. Slices were recorded both parallel and perpendicular to the direction of the fracturing, with an imaging matrix size of 256×256 pixels. After imaging, a Matlab program was used to extract the height profiles from the MRI slices. We used two methods for calculating the roughness exponent:

The detrended fluctuation analysis

$$w(l)=\left\langle\left(h'(x)-\bar{h}'\right)^2\right\rangle_L^{1/2}\propto l^{\zeta},$$

where $h(x)$ is the one-dimensional height profile of the surface, and l is a length along the surface (with total length L); and a Fourier transform method

$$\begin{aligned}C(r)&=\left\langle\left(h(x)-\bar{h}\right)\left(h(x+r)-\bar{h}\right)\right\rangle\\ S(\omega)&=\left|\mathrm{Ftr}\ C(r)\right|^2\propto\omega^{-(1+2\zeta)}\end{aligned},$$

where $C(r)$ is the height-height correlation function, and Ftr means Fourier transform. The results below are an average of the two methods. Further information about the methods can be found e.g. in Bouchaud [2]. To compensate for errors caused by finite size effects and low resolution, we also corrected the calculated ζ 's based on the results presented in Bakke et al. [8].

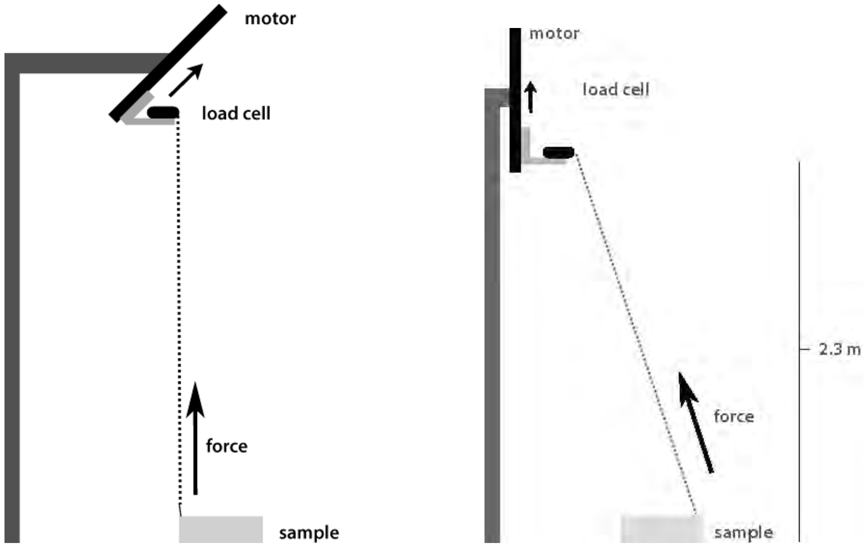

Figure 2

The setups used for fracturing. a) Pure Mode-I. b) Mixed Mode-I and Mode-II.

We used two different motor setups to create the fracture surface. With the setup in Figure 2 a), the fracture is a pure Mode-I fracture, and the results in Figure 3 a) show that we find roughness exponents close to 0.5 for all fracturing velocities. There seems to be no difference in roughness parallel and perpendicular to the fracturing direction.

With the setup shown in Figure 2 b), we are using a combination of Mode-I and Mode-II fracturing, and the results [Figure 3 b)] seem to indicate that the roughness in the transversal direction depends on the fracturing velocity. The results from the parallel direction are omitted, because large-scale bumps on the surface caused by this fracturing setup complicate the analysis.

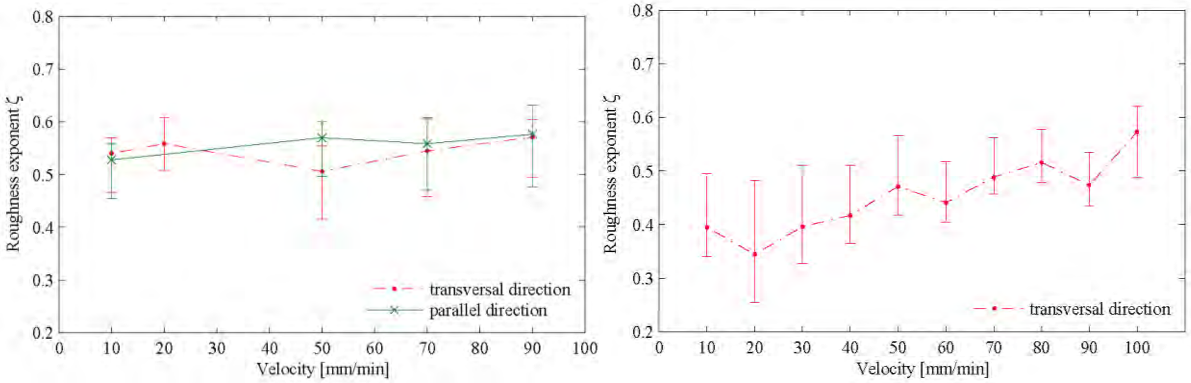

Figure 3

Calculated roughness exponents. a) Results from the pure Mode-I fracture. b) Results from the mixed Mode-I and Mode-II fracture.

It seems natural to assume that the velocity dependence in Figure 3 b) is caused by the in-plane shear involved in the Mode-II fracturing. Unfortunately there are few studies of mixed mode fractures in the literature due to the complexity of the fracture mechanics with such setups. Attempting a qualitative explanation, we can consider the persistence [9] of the Laponite gels. A persistent surface ($\zeta > 1/2$) has the property that it is most probable that any given step in a height profile will go in the same direction as the previous step. Oppositely, a step in the height profile of an antipersistent surface ($\zeta < 1/2$) will change direction more often than not. We see from Figure 3 b) that the roughness of the Laponite surface goes from being antipersistent at low velocities to persistent at high velocities. Due to the shear-thinning properties of Laponite gels [10], we find it reasonable that that the clay gel possesses properties that are suppressed at high pulling speeds, but that leads to antipersistency when the velocity is low. In fact, just by considering the shear-thinning itself, a velocity- dependent roughness makes sense, as we would expect the roughness to decrease with decreasing viscosity.

To conclude, we believe that this is the first time the roughness exponent has been found for fractures in clay gels. Although the Hurst exponent has previously been found from MRI images in texture analysis [11], we also believe this is the first time MRI has been used to find the roughness of self-affine fracture surfaces. The drawback of the method is the limited resolution and long image acquisition times, both of which can probably be improved from this first attempt.

Acknowledgements

The authors thank CNPq, Brazil and the Research Council of Norway. We also thank UFPE, Brazil and NTNU, Norway for support.

References

[1] P. Meakin, *The Growth of Rough Surfaces and Interfaces*, Phys. Rep., 235, 189 (1993)

[2] E. Bouchaud, *Scaling properties of cracks*, J. Phys.: Condens. Matter, 9, 4319 (1997)

[3] B. N. J. Persson, O. Albohr, U. Tartaglino, A. I. Volokitin, and E. Tosatti, *On the nature of surface roughness with application to contact mechanics, sealing, rubber friction and adhesion*, J. Phys.: Condens. Matter, 17, R1 (2005)

[4] A. Mourchid, E. Lecolier, H. Van Damme, and P. Levitz, *On viscoelastic, birefringent, and swelling properties of Laponite clay suspensions: Revisited phase diagram*, Langmuir, 14, 4718 (1998)

[5] A. Mourchid, A. Delville, J. Lambard, E. Lecolier, and P. Levitz, *Phase-Diagram of Colloidal Dispersions of Anisotropic Charged-Particles - Equilibrium Properties, Structure, and Rheology of Laponite Suspensions*, Langmuir, 11, 1942 (1995)

[6] Rockwood Additives Ltd. Laponite – Performance additives. www.scprod.com/pdfs/LaponiteBrochureE.pdf (2007-10-04)

[7] Y. Tanaka, K. Fukao, and Y. Miyamoto, *Fracture energy of gels*, Eur. Phys. J. E, 3, 395 (2000)

[8] J. O. H. Bakke and A. Hansen, *Accuracy of roughness exponent measurement methods*, Phys. Rev. E, 76, (2007)

[9] J.-F. Gouyet, *Physics and fractal structures* (Springer, New York, 1996).

[10] B. Abou, D. Bonn, and J. Meunier, *Nonlinear rheology of Laponite suspensions under an external drive*, J Rheol, 47, 979 (2003)

[11] C. Y. Wen and R. Acharya, *Self-similar texture characterization using a Fourier-domain maximum likelihood estimation method*, Pattern Recogn Lett, 19, 735 (1998)

Nanoparticle induced multi-vesiculation of phospholipid tubes

Irep Gözen[1], Pascale Roux[2], Celine Billerit[1], Paul Dommersnes[1,3,4],
Owe Orwar[1] and Aldo Jesorka[1*]

[1] Chalmers University of Technology, Chemical and Biological Engineering, SE-412 96 Göteborg, Sweden, [2] Sanofi S.A., 371 rue du prof Blayac 34374 Montpellier cedex 04., France,[3]Matieres et Systemes Complexes, Universite Paris Diderot, Paris, 75013, France, [4]Centre for Advanced Study at The Norwegian Academy of Science and Letters, Oslo, Norway

Contact email: aldo@chalmers.se

Biological membrane tubes fulfill important functions within biological cells, e.g. supplying components, conducting signals and transporting virus particles and bacteria. Many functions are still insufficiently understood, which has placed these nanostructures into the focus of recent investigation. We report here on our observations of transient tubulation in nanoparticle-containing, flat giant unilamellar vesicles (FGUVs) on SiO_2*.*

Biological nanotubes are hollow cylindrical biomembrane structures which are typically 50–200 nm in diameter and up to several hundred micrometers long. They occur naturally both in plant[1] and animal cells[2]. By interconnecting animal cells, tunneling nanotubes (TNTs) accomplish important functions, for instance exchanging cytosolic components and organelles[2]. TNTs are known to spontaneously emerge from cells as a response to stress factors[3]. They mediate bidirectional electrical signals up to a distance of 70 micrometers[4] which may point to alternative means of communication between nerve cells. Virus particles which adhere to the outer surface of cell membranes were observed to induce membrane invaginations, e.g., membrane nanotubes, that grow to the interior of the cell[5]. Lipid nanotubes are also present within cells, forming the endoplasmic reticulum[6] and the Golgi apparatus[7]. Mimics of such networks can be created artificially by means of micromanipulation techniques[8] .

Many functions of lipid tubes in cells are still not well understood, which has moved these nanostructures into the focus of recent investigation. The complexity of the plasma membrane makes it challenging to study the impact of individual chemical and physical stimuli on the formation and the function of the tubes. This complexity can be reduced by using model systems, which consist of a known phospholipid composition, often together with other incorporated molecules of interest[9-11]. By using flat giant unilamellar phospholipid vesicles (FGUV) on supporting oxide surfaces as a model system, we have shown that semiconductor nanoparticles (20 nm in diameter, biopolymer coated CdSe), when encapsulated in the FGUV in combination with moderate calcium ion concentrations in the ambient solution, lead to the spontaneous formation of phospholipid nanotubes[12] (Figure 1). This process is mainly driven by the gain in line energy overcoming the entropy loss by migration of a (slightly curved) adhered nanoparticle from the flat vesicle membrane into the nanotube. Ewers *et al.*[5] developed a model which gives a detailed description of such a tubulation process.

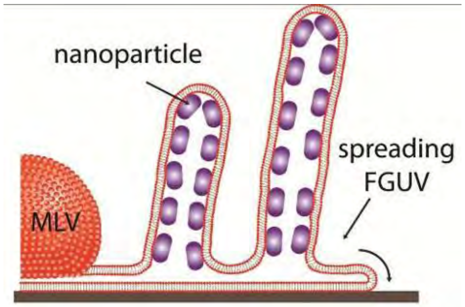

Figure 1
Schematic view of a spreading FGUV with encapsulated nanoparticles, exhibiting tubulation. The drawing is not to scale.

Depending on the increasing tension in the membrane, which is due to the depletion of the MLV, the spreading of the FGUV slows down to a point where the lipid tubes start retracting. We observed that a series of unilamellar vesicles formed inside the tubes, which resulted in sequential multi-vesiculation (Figure 2). This phenomenon is not related to earlier reports of nanotube pearling, where the tube is transformed into a "pearl-chain" of interconnected giant vesicles[13]. In our experiments, the vesicles are encapsulated inside the retracting tube. Reynwar *et al.*[14] have studied by coarse-grain simulations a similar effect on membranes induced by adhering virus capsids and concluded that once an initial curvature was established, the proteins tended to cluster without the involvement of any specific binding, and induced vesiculation of the membrane. This prediction supports our findings, especially regarding the compatibility in size and the well-known tendency of carboxylated nanoparticles to cluster.

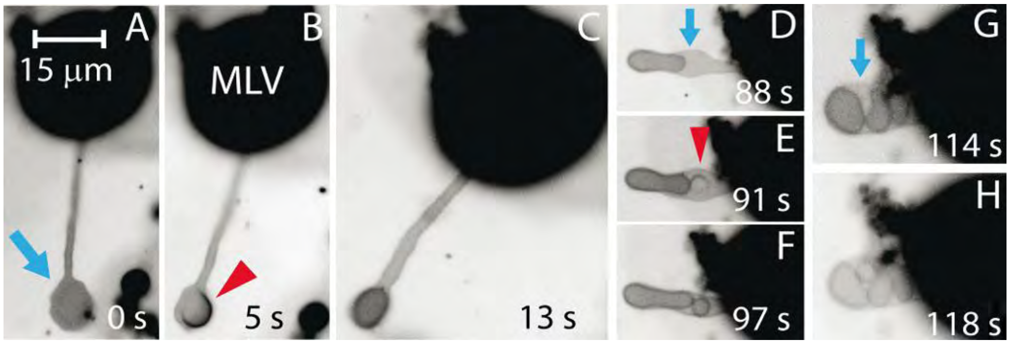

Figure 2
*Time series depicting nanoparticle-induced multi-vesiculation of a phospholipid tube. (**A-H**): The confocal laser scanning time series showing multi-vesiculation of a retracting phospholipid tube emerging from a supported multilamellar vesicle (MLV). (**A**) The formation of a bulge (arrow) at the tube end. (**B**) Unilamellar vesicle (arrow head) emerging from the bulge. (**C**) Completely encapsulated vesicle. (**D**) Formation of a new bulge (blue arrow) in the retracting tube adjacent to the encapsulated vesicle. (**E-H**) Formation of a second (red arrow) vesicle, followed by two more unilamellar vesicles. Fluorescent images were recorded with using a Prosilica GX1920 camera (Allied Vision) and were inverted to enhance contrast.*

The model can support studies on endocytosis, and could potentially be used for the delivery of cargo to cells via nanotubes. The findings need further detailed understanding, focusing on the dynamics of the transformation of the tube bulges into small vesicles at the tube interior.

Acknowledgements: Support was obtained from the European Research Council (ERC), The Swedish Research Council (VR), the Swedish Strategic Research Foundation (SSF) and the Knut and Alice Wallenberg Foundation.

References:

[1] Lucas, W. J., Ham, B. K. & Kim, J. Y. *Plasmodesmata - bridging the gap between neighboring plant cells. Trends in Cell Biology* 19, 495-503 (2009)

[2] Rustom, A., Saffrich, R., Markovic, I., Walther, P. & Gerdes, H. H. *Nanotubular Highways for Intercellular Organelle Transport*. Science 303, 1007-1010 (2004)

[3] Wang, Y., Cui, J., Sun, X. & Zhang, Y. *Tunneling-nanotube development in astrocytes depends on p53 activation. Cell Death and Differentiation* 18, 732-742 (2011)

[4] Wang, X., Veruki, M. L., Bukoreshtliev, N. V., Hartveit, E. & Gerdes, H. H. *Animal cells connected by nanotubes can be electrically coupled through interposed gap-junction channels.* Proceedings of the National Academy of Sciences of the United States of America 107, 17194-17199 (2010)

[5] Ewers, H. et al. *GM1 structure determines SV40-induced membrane invagination and infection*. Nature cell biology 12, 11-18 (2010)

[6] Dreier, L. & Rapoport, T. A. *In vitro formation of the endoplasmic reticulum occurs independently of microtubules by a controlled fusion reaction.* Journal of Cell Biology 148, 883-898 (2000)

[7] Upadhyaya, A. & Sheetz, M. P. *Tension in Tubulovesicular Networks of Golgi and Endoplasmic Reticulum Membranes*. Biophysical Journal 86, 2923-2928 (2004)

[8] Lobovkina, T. et al. *Mechanical tweezer action by self-tightening knots in surfactant nanotubes.* Proceedings of the National Academy of Sciences of the United States of America 101, 7949-7953 (2004)

[9] Sackmann, E. *Supported membranes: Scientific and practical applications.* Science 271, 43-48 (1996)

[10] Czolkos, I., Jesorka, A. & Orwar, O. *Molecular phospholipid films on solid supports*. Soft Matter 7, 4562-4576 (2011)

[11] Lobovkina, T. et al. *Protrusive growth and periodic contractile motion in surface-adhered vesicles induced by* Ca^{2+}*-gradients.* Soft Matter 6, 268-272 (2010)

[12] Gözen, I., Billerit, C., Dommersnes, P., Jesorka, A. & Orwar, O. *Calcium-ion-controlled nanoparticle-induced tubulation in supported flat phospholipid vesicles.* Soft Matter 7, 9706-9713 (2011)

[13] Yu, Y. & Granick, S. *Pearling of lipid vesicles induced by nanoparticles.* Journal of the American Chemical Society 131, 14158-14159 (2009)

[14] Reynwar, B. J. et al. *Aggregation and vesiculation of membrane proteins by curvature-mediated interactions.* Nature 447, 461-464 (2007)

Flux avalanches in superconducting thin films: Frontiers of the instability region

M. Motta[1], F. Colauto[1], T. H. Johansen[2,3,4], R. B. Dinner[5], M. G. Blamire[5], G. W. Ataklti[6], V. V. Moshchalkov[6], A. V. Silhanek[6,7], W. A. Ortiz[1,4]

[1]Departamento de Física, Universidade Federal de São Carlos, 13565-905 São Carlos, SP, Brazil, [2]Department of Physics, University of Oslo, POB 1048, Blindern, 0316 Oslo, Norway, [3]Institute for Superconducting and Electronic Materials, University of Wollongong, Northfields Avenue, Wollongong, NSW 2522, Australia, [4]2011-12: Centre for Advanced Study, Norwegian Academy of Science and Letters, Oslo, Norway, [5]Department of Materials Science, University of Cambridge, Pembroke Street, Cambridge CB2 3QZ, UK, [6]INPAC - Institute for Nanoscale Physics and Chemistry, Nanoscale Superconductivity and Magnetism Group, K.U.Leuven, Celestijnenlaan 200D, B-3001 Leuven, Belgium, [7]Département de Physique, Université de Liège, B- 4000 Sart Tilman, Belgium.

Contact email: wortiz@df.ufscar.br

Under certain conditions of temperature and magnetic field, sudden flux bursts develop into superconducting films. This phenomenon is a consequence of thermomagnetic instabilities, which occur when heat dispersion is slower than magnetic diffusion. The present work reports a systematic study conducted on a Nb film, in which we have determined the frontiers of the flux avalanche regime in the field-temperature diagram, using different approaches based on magnetic measurements. Our results reveal that the instability region determined using ac susceptibility is wider than its equivalent mapped using dc magnetization.

Superconductivity is a macroscopic quantum state in which materials exhibit two mostly distinguishing properties: the ability of carrying zero-voltage supercurrents, and the screening of magnetic fields, the so-called Meissner-Ochsenfeld effect. In type-II superconductors, such screening is complete for fields up to a characteristic value, H_{c1}, above which flux progressively penetrates into the sample. Although apparently continuous, such penetrated flux is quantized, in flux packages of $\Phi_0 = h/2e$, corresponding to the ratio between Planck's constant and the charge carried by a Cooper pair. These entities, carrying typically one flux quantum each, were first predicted in 1957 by Alexei Abrikosov [1], one of the Nobel Laureates in 2003. Vortices were first visualized in 1967, in a Bitter decoration experiment conducted by Essmann and Trauble on a sample of Pb-4at%In [2], and have been ever since thoroughly investigated and visualized by a variety of techniques [3-10].

Even though magnetic flux is quantized in the interior of a type-II superconductor, it is frequently convenient to treat it as a continuous media, by means of the so-called Critical State (CS) models [11], based on the concept that a superconductor will always react to flux entry or exit by means of screening currents, carrying the largest possible density, known as the critical current, J_c. In other words, if a screening current exists in any place of a sample in a CS regime, its value is that of the sample's critical current. The original - and simplest - CS model was proposed by Bean [12,13], in which J_c is independent of the local magnetic field. This apparent oversimplification, however, works very well in many practical circumstances, for which J_c represents an effective value of the critical current density throughout the sample. As will be discussed later in this paper, a number of relevant links between J_c and magnetic properties -

e.g., magnetization loops and ac-susceptibility measurements - can be derived for samples obeying the Bean CS model.

The smooth penetration of magnetic flux into a type-II superconductor is a quite general behavior, both in bulk samples and thin films. In spite of this, it has been widely observed that, under certain conditions of temperature, *T*, and magnetic field, *H*, sudden flux avalanches develop into superconducting films [14], as a consequence of thermomagnetic instabilities, which result from a competition between the fast magnetic diffusion, related to flux movement throughout the sample, and the sample capability to disperse heat generated by such a viscous motion.

These avalanches have been detected and studied using magnetization and susceptibility measurements, as well as magneto-optical imaging (MOI) [15-18]. Arguably, being able to see such avalanches directly, through use of MOI, has been an invaluable aid in the study and thorough understanding of the thermomagnetic instabilities which underlie such catastrophic occurrences. The observation of flux avalanches triggered by thermomagnetic instabilities have been reported in a variety of superconducting films of Nb [18-20], MgB_2 [15,17,21], Nb_3Sn [22], NbN [23], YNi_2B_2C [24], YBCO [25], and a-MoGe [26].

In recent years, some of the present authors have contributed to establish quantitative links among some of the most useful tools employed on the investigation of flux avalanches, such as MOI and magnetic measurements (MMs), including the field and temperature dependence of the magnetic moment [17], as well as the corresponding dependences of the ac-susceptibility [18]. In addition, isothermal measurements of the latter as a function of the excitation field amplitude, taken at a constant applied dc-field, can also give important information regarding obedience of the Bean model, through investigations of the so-called Cole-Cole plots and, if so, determination of J_c [27-30].

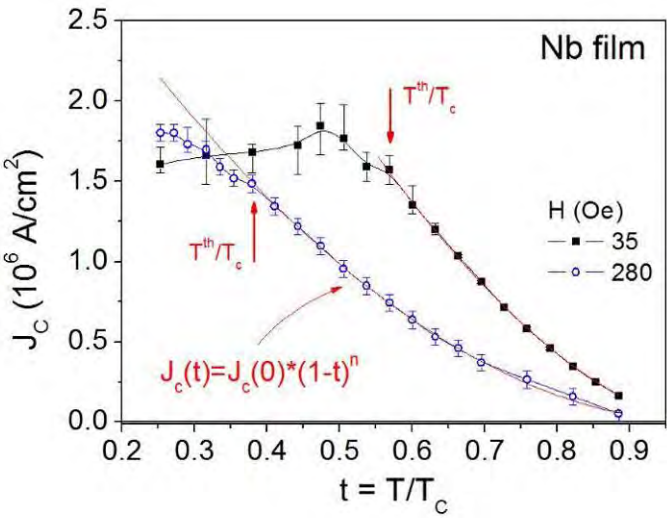

Figure 1
Temperature dependence of the critical current density at two different values of the applied magnetic field. The threshold temperatures below which avalanches occur are indicated by the vertical arrows.

This paper reports briefly on the use of magnetization and ac-susceptibility to determine, in the *HT*—diagram, the frontiers of the instability region within which flux avalanches occur in Nb films. The sample investigated in the present work consists of a Nb film of approximately rectangular shape, with lateral dimensions 2.5x3.0 mm^2 and thickness 50 nm, deposited on a SiO_2 insulating substrate. Its superconducting transition temperature at zero magentic field is T_c = 7.91 K. Characterization measurements of the ac susceptibility and dc magnetization were carried out in commercial Quantum Design equipments (MPMS and PPMS). Susceptibility measurements were made at a fixed frequency of 1 kHz, with excitation fields not exceeding 15 Oe. The excitation field h and the dc magnetic field were always applied parallel to each other and perpendicular to the film plane.

The Bean model has been studied for many decades, and a vast literature exists relating all aspects of the magnetic response of a superconducting sample and its critical current density. Our approach involves measuring the value h_p of the excitation field at which the imaginary part of the ac-susceptibility is maximum [31]. As previously discussed by Shantsev and coauthors [32], above a certain value of the applied field - which is characteristic of the sample - the Bean model can be used without restrictions for superconducting thin films. For the sample studied here, the characteristic field is around 20 Oe [18], above which our experimental window starts.

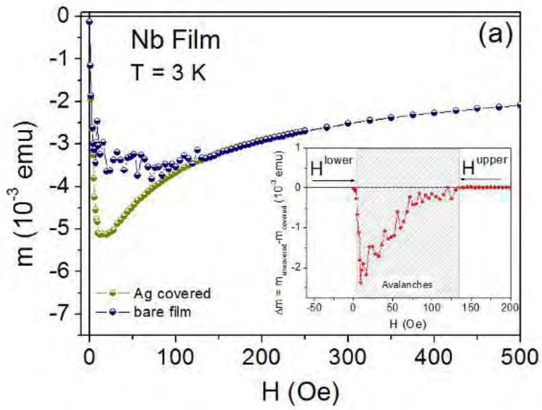

Figure 2

(a) Magnetic moment versus applied field measured at a temperature within the thermoinstability region, with and without a silver disk, placed in close contact with the film in order to suppress avalanches. The difference between both curves is shown in the inset.

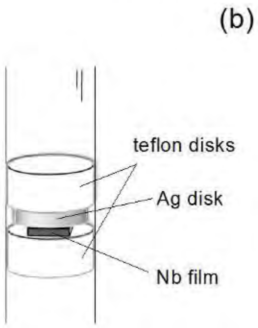

(b) Sketch of the sample assembly with the silver disk.

Figure 1 shows how J_c varies with the reduced temperature, $t=T/T_c$, for two different values of the applied filed. Apparent in the graph is the occurrence of two different regimes: at higher temperatures, J_c is a smooth decreasing function of T, whereas in the lower temperature regime it is noisy and much less sensitive to T. The reason for the existence of this crossover among regimes is the appearance of avalanches at lower temperatures. In reality, values of J_c shown for temperatures below the avalanche threshold do not represent the critical current density, since they were obtained under the wrong assumption that the system is in a critical state regime. Contrarily, in the avalanche regime the actual critical current is a local, extremely inhomogeneous variable, which cannot be properly described by a unique global value. However, displaying all points in a single picture is quite useful, not only to show the existence of a frontier between both regimes, but also to allow for its precise determination, what is done by fitting the power-law expression shown in the graph. The threshold temperature, T_{th}, is obtained as the lowest value of T for which the corresponding J_c pertains to the fitted curve, as indicated by the arrows in Fig. 1. It should be noticed that, for a given value of the applied field, T_{th} is the maximum temperature for which avalanches develop, being thus the upper limit of the instability region. Repeating this procedure for different values of *H* one can then determine the upper boundary of such regime.

On the other hand, the occurrence of avalanches can also be detected in isothermal measurements of the field-dependence of the magnetic moment of the film [16,17], as illustrated in Figure 2a for the sample studied here. The main graph also shows a magentization versus field curve taken with the sample covered by a disk of Ag, which constitutes an efficient way to suppress avalanches, as has been demonstrated by Baziljevich et al. [33], and discussed in detail by Colauto and coworkers [34]. The scketch of the sample mounting is shown in Figure 2b.

We have used the difference between both curves – i.e., Ag-covered and bare film – to determine the lower and upper thresholds of the instability region, represented in the inset by H^{lower} and H^{upper}, respectively.

Figure 3 shows the *HT*–diagram, including the TMI region determined by dc experiments, as discussed in the previous paragraph. It also includes the upper threshold obtained using ac susceptibility measurements, as delineted earlier in this paper. In spite of the similar trend exhibited by the two versions of the upper frontier, a considerable difference exists (notice the logarithmic scale of the vertical axis) between them. The reason for this difference derives from the fact that, even in the absence of an applied dc field, the ac field employed to excite the sample in susceptibility measurements – if sufficiently strong – can trigger avalanches, as has been already detected in previous publications [35,36] and formally demonstrated recently [18]. It is also worth mentioning that, in a recent work on a NbN film, Qviller and coworkers [37] reported that the frontier of the instability region, determined from zero-field cooled MOI experiements (corresponding to the virgin curve of a hysteresis loop), does not match the corresponding boundary obtained from field-cooled runs. These results are consistent with the findings reported here. Additional studies on this subject are being conducted and will appear elsewhere.

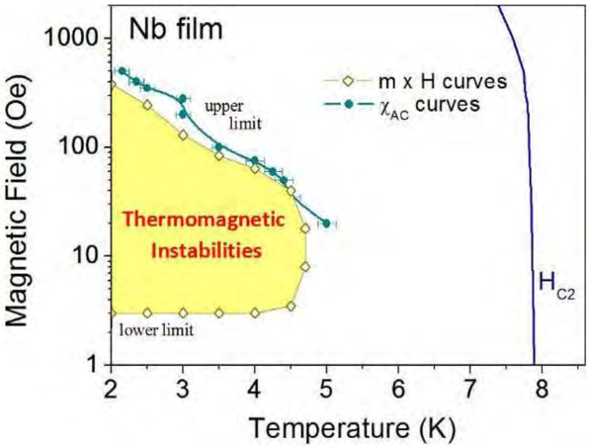

Figure 3
HT–phase diagram showing the region dominated by thermomagnetic instabilities, as determined by dc (magnetic moment) and ac (susceptibility) techniques.

Acknowledgements

Work partially supported by the Methusalem Funding of the Flemish Government, the NES-ESF program, the Belgian IAP, the Fund for Scientific Research-Flanders (FWO-Vlaanderen), the

UK Engineering and Physical Sciences Research Council and the Brazilian funding agencies FAPESP and CNPq. AVS is grateful for the support from the FWO-Vlaanderen.

References

[1] A. A. Abrikosov, Sov. Phys. JETP 5, 1174 (1957)
[2] U. Essmann and H. Trauble, Physics Letters A 24, 526 (1967)
[3] P. Gammel, D. J. Bishop, G. J Dolan et al., Phys. Rev. Lett. 59, 2592 (1987)
[4] H. F. Hess, R. B. Robinson, R. C. Dynes, et. al., Phys. Rev. Lett. 62, 214 (1989)
[5] K. Harada, T. Matsuda, J. Bonevich, et. al, Nature 360, 51 (1992)
[6] K. Harada, O. Kamimura, H. Kasai, et al., Science 274, 1167 (1996)
[7] P. E. Goa, H. Hauglin, M. Baziljevich, et al., Superconductor Science and Technology 14, 729 (2001)
[8] M. R. Eskildsen, M. Kugler; S. Tanaka, et al., Phys. Rev. Lett. 89, 187003 (2002)
[9] A. Volodin, K. Temst, C. Van Haesendonck, et al., Europhysics Letters 58, 582 (2002)
[10] L. Y. Vinnikov, J. Karpinski, S. M. Kazakov, et al., 67, 092512 (2003)
[11] A. M. Campbell and J. E. Evetts, Adv. Phys. 21, 199 (1972)
[12] C. P. Bean, Phys. Rev. Lett. 8, 250 (1962)
[13] C. P. Bean, Rev. Mod. Phys. 36, 31 (1964)
[14] E. Altshuler and T. H. Johansen, Rev. Mod. Phys. 76, 471 (2004)
[15] T. H. Johansen et al., Europhys. Lett., 59, 599 (2002)
[16] Eun-Mi Choi et al., Appl. Phys. Lett. 87, 152501 (2005)
[17] F. Colauto et al., Supercond. Sci. Technol. 20, L48 (2007)
[18] M Motta et al., Phys. Rev. B 84, 214529 (2011)
[19] C. A. Duran et al., Phys. Rev. B 52, 75 (1995)
[20] V. Vlasko-Vlasov, U. Welp, V. Metlushko, and G. W. Crabtree, Physica C 341, 1281 (2000)
[21] T. H. Johansen et al., Supercond. Sci. Tech. 14, 726 (2001)
[22] I. A. Rudnev et al., Cryogenics 43, 663 (2003)
[23] I. A. Rudnev, D. V. Shantsev, T. H. Johansen, A. E. Primenko, Appl. Phys. Lett. 87, 042502 (2005)
[24] S. C. Wimbush, B. Holzapfel, and C. Jooss, J. Appl. Phys. 96, 3589 (2004)
[25] P. Leiderer et al., Phys. Rev. Lett. 71, 2646 (1993)
[26] M. Motta et al., arXiv:submit/0316943 [cond-mat.supr-con] 12 Sep 2011
[27] E. H. Brandt and M. Indenbom, Phys. Rev. B 48, 12893 (1993)
[28] E. Zeldov, J. R. Clem, M. McElfresh, and M. Darwin, Phys. Rev. B 49, 9802 (1994)
[29] J. R. Clem and A. Sanchez, Phys. Rev. B 50, 9355 (1994)
[30] D.-X. Chen, C. Navau, N. Del-Valle, and A. Sanchez, Physica C 470, 89 (2010)
[31] For a thorough discussion of the method and the choice of the expression valid for the rectangular sample employed here, see Ref. 30.
[32] D. V. Shantsev, Y. M. Galperin, T. H. Johansen. Phys. Rev. B 61, 9699 (2000)
[33] M. Baziljevich et al., Physica C **369**, 93 (2002)
[34] F. Colauto et al., Appl. Phys. Lett. 96, 092512 (2010)
[35] A. V. Silhanek, S. Raedts, and V. V. Moshchalkov, Phys. Rev. B **70**, 144504 (2004)
[36] M. Menghini et al., Phys. Rev. B **71**, 104506 (2005)
[37] A. J. Qviller et al., Physica C 470, 897 (2010)

Synchrotron X-ray scattering studies of Li-Fluorohectorite synthetic clay: Random intercalation states

L. E. Michels[1], H. Hemmen[2], R. Droppa Junior[3], G. Grassi[1], G. J. da Silva[1]and J. O. Fossum[2,4].

[1]Instituto de Física, Universidade de Brasília, IF-UnB, Brasília-DF, Brasil, [2]Department of Physics, Norwegian University of Science and Technology, NTNU, Trondheim, Norway, [3]Centro de Ciências Naturais e Humanas, Universidade Federal do ABC, UFABC, São Paulo-SP, Brasil, [4]2011-12: Centre for Advanced Study – CAS, at the Norwegian Academy of Science and Letters, Oslo, Norway

Contact e-mail: leander@fis.unb.br

Synchrotron x-ray diffraction studies were performed on synthetic layered silicate Li-Fluorohectorite clay. Diffraction patterns along the stacking direction were obtained in bulk transmission with controlled temperature as a function of relative humidity. In the present study emphasis is on the transition peaks in between two hydration states which are associated to Hendricks-Teller like peaks.

Introduction

Li-Fluorohectorite (Li-Fh) is a 2:1 layered phyllosilicate clay. Its basal structural unit is formed by two inverted silicate tetrahedral sheets, sharing their apical oxygen with one octahedral sheet sandwiched in between, see Fig 1. It has the chemical formula per half unit cell $Li_x-(Mg_{3-x}Li_x)Si_4O_{10}F_2$, where the proportion x of the Li^+ ions determines the layer charge of the platelets, which are held together in a stacked structure by an interlayer cation.

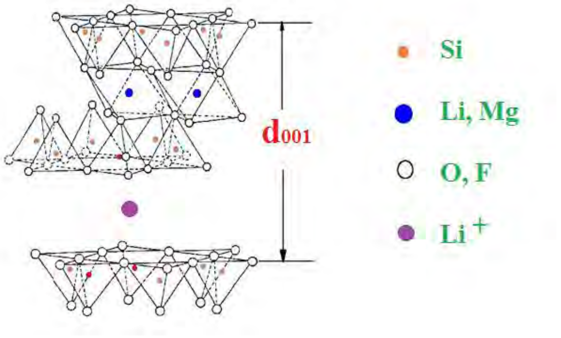

Figure 1
Diagram of the Li-Fh clay structure.

Water can be intercalated in between each platelet causing the clay to swell. This intercalation process, which can be controlled by temperature and relative humidity, yields stable hydration states which are quite well ordered along the stacking direction. The unit cell along the stacking direction is given by the repetition distance '*d*' between the stacked platelets, and for Li-Fh it is around 1.0 nm for the case of 0 water layers (WL) and 1.2, 1.4, 1.6 and 1.8 nm for the cases of one, one and half, two and three water layers respectively [1]. In addition there can be random intercalation states present in such systems possibly resulting in so-called Hendricks-Teller scattering peaks [2].

The main objective of the present study is to map out the distance d_{001} as a function of *relative humidity* (RH) in Li-Fh, at fixed temperature, and look for Hendricks-Teller peaks at the transitions between hydration states. The temperature was kept constant by pumping water, from a water bath, through a copper base in contact with the sample holder. Scans were done around the 001 stacking peaks and fitted with Voigt profiles in order to get the d-spacing.

Experiment preparation

Li-Fh powder is put inside the sample cell: a small hole in a copper piece, kept inside a closed cylinder together with the humidity sensor. We pump humidity-regulated air into this chamber. The regulation of humidity is done by combining air from a dry source (pure nitrogen) and nitrogen pumped through water and controlled by a flowmeter, see Figure 2. By controlling the respective fluxes from the two sources and merging them before entering the sample chamber the varying humidity is obtained. A humidity sensor *Sensirion* model*BT7-71* is used to measure the humidity.

The x-ray scattering measurements were conducted at beamline XRD1 at the National Synchrotron Light Source - LNLS [3], using an x-ray wavelength of 0.124 nm, and a focused beam spot about 0.4 mm high and 0.5 mm wide.

In this experiment the relative humidity was monotonically increased from 0% to 90% at a constant temperature of 25°C. After each small increase in the humidity, the sample was left to equilibrate for 15 minutes. The humidity and temperature were measured before and after each x-ray scan. Any decrease in the humidity was avoided since it can cause hysteresis.

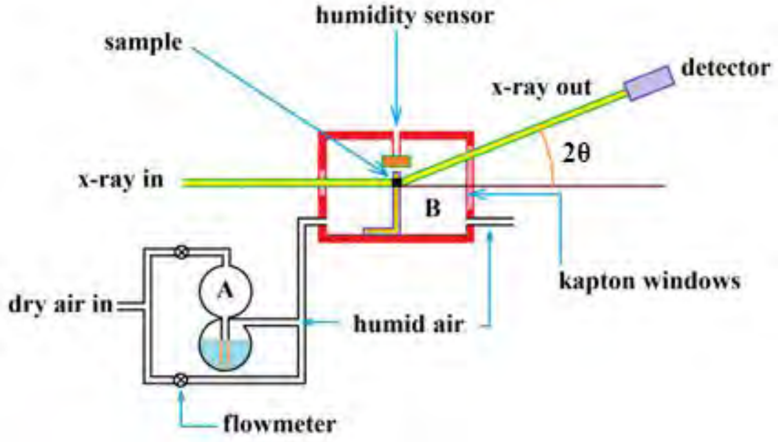

Figure 2

A sketch of the experimental setup showing the system of humidity generation (A) and the sample chamber (B).

Experimental Results and Data Analysis

Figure 3 shows two x-rays scattering profiles at different humidity. For the analysis of the peaks, we consider the measured intensity I(q) dependent of the Lorentz-polarization factors $L_P(q)$ and of the interference function $\Phi(q_0, \Omega_G, \Omega_L)$ given by

$$I(q) \propto L_p(q_0)\,\Phi(q_0, \Omega_G, \Omega_L) \qquad (1)$$

where $q_0 \equiv q - q_c$, and $q \equiv 4\pi \sin\theta / \lambda$ is the x-ray scattering vector modulus, and q_c is the peak position related to the basal distance by

$$q_c = \frac{2\pi}{d_{001}} \qquad (2)$$

Lorentz-polarization factors 'L_p' were calculated according to reference [4]. The Voigt profile is a convolution of a Lorentz $L(q_0, \Omega_L)$ and a Gaussian $G(q_0, \Omega_G)$ profile, both centered at q_c, and defined by

$$\Phi(q_0, \Omega_G, \Omega_L) = \int_{-\infty}^{\infty} L(q_0 - q', \gamma) G(q', \Omega_G)\, dq' \qquad (3)$$

The Lorenz and the Gaussian curves are respectively associated with the pure line profile and the experimental resolution.

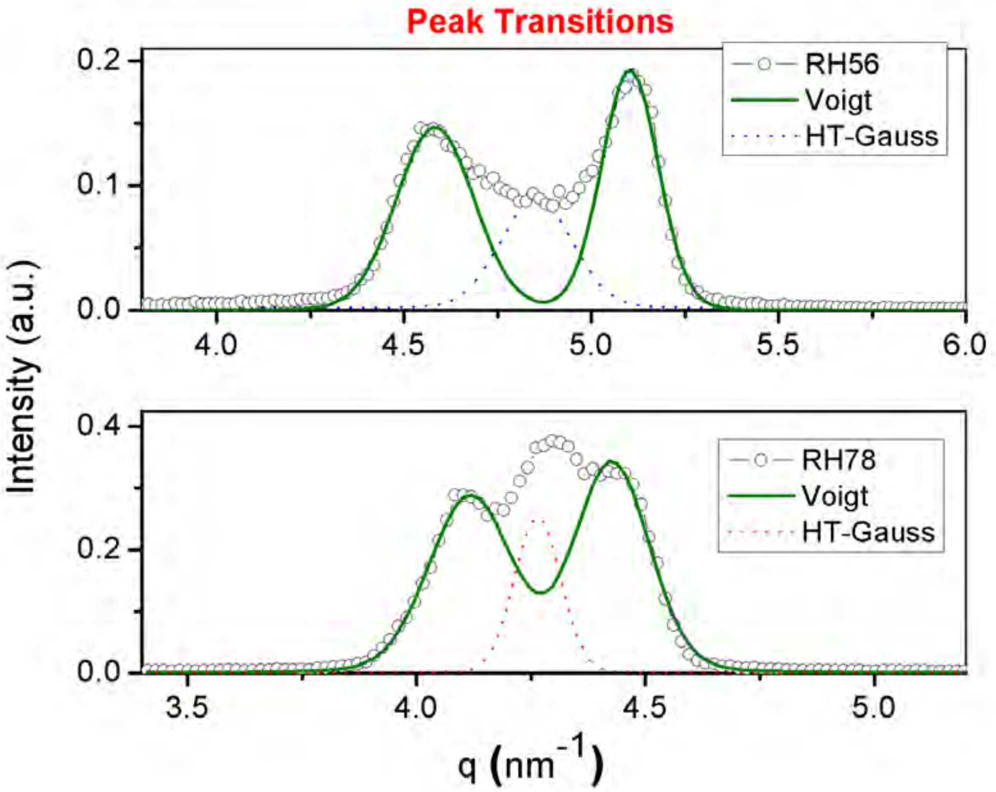

Figure 3

(Top) Relative humidity of 56% , corresponding to a transition between 1WL and 1.5WL. (Bottom) Relative humidity of 78%, corresponding to a transition between 1.5WL and 2WL. The Gaussian peaks fitted considered to be random mixture of pure Hendrix-Teller peaks (dot lines).

The peaks centered at 5.2 nm^{-1} and 4.6 nm^{-1} represent the 1 and 1.5 water layer hydration states [4], respectively, and the peak at 4.1 nm^{-1} is associated with the 2 water layers regime. When the humidity in the sample changes, the peak positions move due to small variations in d-spacing [5]. In a limited range of humidities around the transition between two hydration states, the two states involved in the transition coexist. In such mixed regimes we also observe additional scattering between the pure hydration peaks, which is known as Hendricks-Teller-like peaks [4]. A Gaussian function, not related with the Voigt convolution, was used to fit this scattering, because the observed Hendricks-Teller peaks in reality are due a random mixture of "pure" Hendricks-Teller peaks. The evolution of the fitted Gaussian as a function of the humidity is then converted to d-distance in a similar way as for the pure diffraction peaks.

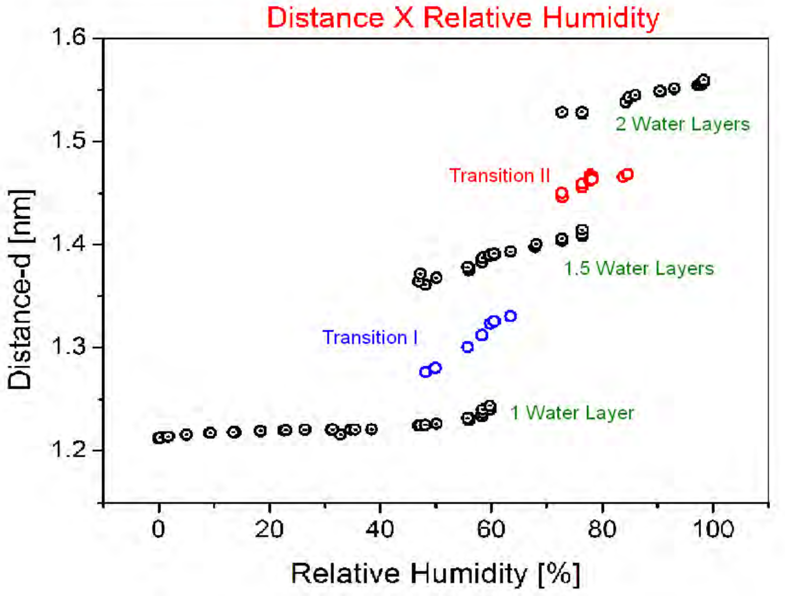

Figure 4

d-spacing as a function of relative humidity. Black dots refer to stable water layer hydration states and those named transition I and II refer to the Hendricks-Teller-like peaks.

Figure 4 shows the coexistence of different water layer states with emphasis on the peak in between the pure hydration states. This peak is regularly observed during the transition between hydration states, and was previously observed in Na-Fluorohectorite [4], which has Na^+ as interlayer cation instead of Li^+, resulting in slightly different stable hydration states. Meanwhile to quantify this phenomenon further, it is necessary to investigate the transition behavior also for higher order peaks. That is the subject of another ongoing work.

Acknowledgements

This work has been supported by Coordenação de Aperfeiçoamento de Pessoal de Nível Superior (CAPES) and Laboratório Nacional de Luz Sincrotron (LNLS), the Norwegian University of Science and Technology (NTNU) and the Research Council of Norway (NFR). *L. E. Michels* wishes to acknowledge the support from Vice-Reitoria (VcR/UnB) and Instituto de Física (IF/UnB),

References

[1] Tenório, R. P.; Engelsberg, M.; Fossum, J. O.; da Silva, G. J. ; *Langmuir*, **26**(12), 9703(2010)
[2] S. Hendricks and E. Teller, J. Chem. Phys. 10, 147 (1942)
[3] Project LNLS#10795 - XRD1 –'*Self-organization of synthetic clay particles in droplet deposits*'.
[4] da Silva, G. J.; Fossum, J. O.; DiMasi, E.; Maløy, K. J.; Lutnæs, S. B. *Phys. Rev. E*, **66**, 011303 (2002)
[5] Hemmen, H.; Alme, L.R.; Fossum, J.O.; Meheust, Y. *Phys. Rev. E*, **82**, 036315 (2010)

Hamiltonian for a point vortex around a circular cylinder near a plane boundary

M. N. Moura and G. L. Vasconcelos

Laboratório de Física Teórica e Computacional, Departamento de Física, Universidade Federal de Pernambuco, 50670-901, Recife, Brazil

Contact e-mail: marcelmoura@yahoo.com.br

The dynamics of vortices in a fluid surrounding multiple solid obstacles is of great theoretical interest and practical importance. In particular, the case of vortex motion in a fluid past a circular cylinder placed above a plane wall has attracted considerable attention recently. In this case, a stationary vortex is formed upstream of the cylinder, as found in experiments by Lin et al. [1]*, in contradistinction to the usual case without the plane where a vortex pair is observed behind the cylinder* [2]. *In the present work, the motion of a point vortex in an ideal fluid flow past a circular cylinder placed above a plane boundary is studied analytically. Using complex analysis techniques devised by Crowdy and Marshall* [3] *to analyze vortex dynamics in multiply connected domains in two-dimensional potential flows, we obtain the Hamiltonian for the problem of one point vortex placed in a uniform stream past a circular cylinder above a plane. The corresponding phase portrait is obtained.*

The formation of vortices around solid obstacles is a very common fluid dynamical event. At moderate Reynolds numbers one can easily observe the presence of a pair of counter-rotating vortices downstream of a circular cylinder placed in a uniform flow. This system was first studied analytically by Föppl in 1913 [2] using a point vortex model. The use of this lower dimensionality model is still widely employed to treat vortex dynamics, since, despite its simplicity, it can capture several of the main features of real systems [4,5].

Although the dynamics of vortices around a single solid boundary has been studied for several different systems [6,7], the analysis of problems in which more than one boundary is present is very sparse in the literature. Here we study the motion of a point vortex of intensity Γ in a uniform stream of velocity U past a circular cylinder of radius s, whose center lies at a distance d from a plane; see Figure 1. The main purpose of this paper is to present for the first time the Hamiltonian for this system.

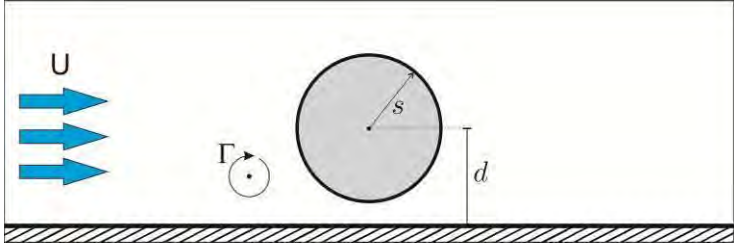

Figure 1
One vortex in a uniform stream past a circular cylinder above a plane.

Since the fluid domain is not simply connected, we will employ a recently developed mathematical technique which makes use of the so-called Schottky-Klein prime function to compute the Hamiltonian governing the dynamics of the system. This method was devised by Crowdy and Marshall in 2005 [3] and can, in principle, be used to analyze the motion of point vortices around any arbitrary set of obstacles. As a first step to compute the Hamiltonian, let us calculate the complex potential associated with the flow of one point vortex in this multiply connected domain. The complex potential is a complex function $w = \phi + i\psi$ whose real and imaginary parts are, respectively, the velocity potential ϕ and the streamfunction ψ associated with the flow. The complex potential is a very useful mathematical tool in the analysis of incompressible potential flows, as the one studied here. As is well known [6], the complex potential for a point vortex of unit intensity at the position $z = z_v$, in the region outside of a circular cylinder placed in an otherwise unbounded domain can be written as

$$w\left(z, z_v\right) = \frac{1}{2\pi i} \log\left[\frac{z - z_v}{z - 1/\bar{z}_v}\right], \tag{1}$$

where the numerator in the log is due to the vortex itself and the denominator is due to the vortex image in the unphysical region (inside the cylinder).

In the case of systems involving more than one boundary, it is not straightforward to obtain the complex potential, since the vortex images are not trivially calculated. Therefore, we have to make use of a different method to handle vortex flows in multiply connected domains. To this end, it is necessary first to introduce a circular domain in an auxiliary complex ζ plane, which will be conformally mapped onto the physical domain in the complex z plane. In the case studied here, where the boundaries are a cylinder and a plane, this circular domain is the annulus $r_0 \le |\zeta| \le 1$, as shown in Figure 2, where

$$r_0 = \frac{1 - \sqrt{\dfrac{d - s}{d + s}}}{1 + \sqrt{\dfrac{d - s}{d + s}}}. \tag{2}$$

The conformal map $z(\zeta)$ and its inverse $\zeta(z)$ are given by,

$$z(\zeta) = -i\sqrt{d^2 - s^2}\,\frac{\zeta - i}{\zeta + i}, \qquad \zeta(z) = -i\,\frac{z - i\sqrt{d^2 - s^2}}{z + i\sqrt{d^2 - s^2}}. \tag{3}$$

According to Refs. [3] and [8], in the multiply connected case, the complex potential $w(\zeta, \alpha)$ for a point vortex of unit intensity, at the position $\zeta = \alpha$ in the auxiliary complex ζ plane, is given by

$$w\left(\zeta, \alpha\right) = \frac{1}{2\pi i} \log\left[\frac{\omega(\zeta, \alpha)}{|\alpha|\,\omega(\zeta, 1/\bar{a})}\right], \tag{4}$$

where $\omega(\zeta, \alpha)$ is a special function, the so-called Schottky-Klein prime function, which encodes the geometry of the circular domain in the complex ζ plane. In the present case $\omega(\zeta, \alpha)$ is given by [8]

$$\omega(\zeta, \alpha) = -\frac{\alpha}{C} P\left(\frac{\zeta}{\alpha}, r_0\right), \tag{5}$$

where

$$C = \prod_{n=1}^{\infty}\left(1 - {r_0}^{2n}\right) \tag{6}$$

is a constant and

$$P(x, y) = (1 - x)\prod_{n=1}^{\infty}\left(1 - y^{2n}x\right)\left(1 - y^{2n}x^{-1}\right). \tag{7}$$

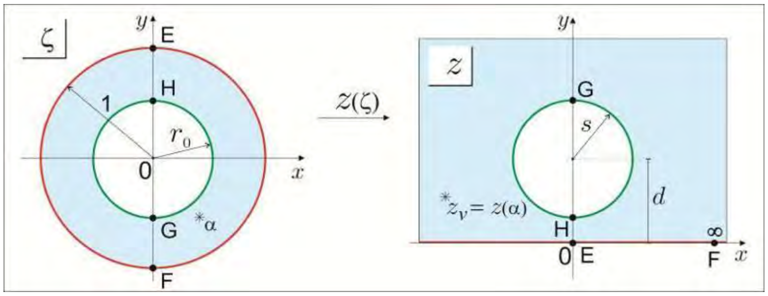

Figure 2
Conformal map between the circular domain in the auxiliary complex ζ plane and the physical domain in the complex z plane.

We now need to consider the contribution from the uniform stream. It is well known [6] that the complex potential for a uniform flow past a cylinder without any other boundaries is given by $w_U(z) = U(z+1/z)$. For systems with more boundaries it is once again necessary to go to the auxiliary ζ plane. In the case studied here, it can be shown [9] that the complex potential due to the uniform flow is given in the ζ plane by

$$w_U(\zeta) = -2\pi U i\sqrt{d^2 - s^2}\left(\frac{\partial w}{\partial \bar{\alpha}} - \frac{\partial w}{\partial \alpha}\right)\bigg|_{\alpha=-i}, \tag{8}$$

where $w(\zeta,\alpha)$ is given in (4). When expressed in terms of the *z* variable, the above potential satisfies the appropriate boundary conditions: both the cylinder and the plane are streamlines of the flow, and at infinity one has a uniform flow with velocity *U*.

To compute the Hamiltonian $H^{(z)}$ in the z plane, it is again more convenient to obtain first the corresponding Hamiltonian $H^{(\zeta)}$ in the ζ plane. Following the general methodology presented in [3], we find

$$H^{(\zeta)}(\alpha,\bar{\alpha}) = \Gamma\psi_U(\alpha,\bar{\alpha}) + \frac{\Gamma^2}{4\pi}\log\left|P\left(|\alpha|^2, r_0\right)\right| \tag{9}$$

where ψ_U is the streamfunction associated with the uniform flow, i.e., the imaginary part of w_U given in (8):

$$\psi_U(\zeta,\bar{\zeta}) = \mathrm{Im}[w_U(\zeta)]. \tag{10}$$

The Hamiltonian, however, is not invariant under a conformal mapping. To calculate the Hamiltonian $H^{(z)}$, it is necessary to add a correction term [10] to the Hamiltonian $H^{(\zeta)}$,

$$H^{(z)}(z_v,\bar{z}_v) = H^{(\zeta)}(\zeta,\bar{\zeta}) + \frac{\Gamma^2}{4\pi}\log\left|\frac{dz}{d\zeta}\right|_{\zeta=\alpha}, \tag{11}$$

In the present case, this correction term reads

$$\frac{\Gamma^2}{4\pi}\log\left|\frac{dz}{d\zeta}\right|_{\zeta=\alpha} = \frac{\Gamma^2}{4\pi}\log\left|\frac{2\sqrt{d^2-s^2}}{(\alpha+i)^2}\right| \tag{12}$$

The Hamiltonian $H^{(z)}$ is obtained by first adding (9) and (12), and then using the inverse map given in (3) to transform back to the *z* variable, recalling that $\alpha = \zeta(z_v)$. Neglecting an additive constant (unimportant to the dynamics), we obtain

$$H^{(z)}(z_v,\bar{z}_v) = \Gamma\psi_U\left(\zeta(z_v), \overline{\zeta(z_v)}\right) + \frac{\Gamma^2}{4\pi}\log\left|\frac{P\left(|\zeta(z_v)|^2, r_0\right)}{(\zeta(z_v)+i)^2}\right|. \tag{13}$$

Since the Hamiltonian is a constant of motion, it is possible to obtain a vortex trajectory by simply making a contour plot of the Hamiltonian. Letting $z_v = x + i\,y$, we have

$$H(x,y) = H^{(z)}(x+i\,y, x-i\,y) = c, \tag{14}$$

where *c* is a constant. Figure 3 shows a set of vortex trajectories (or a phase portrait of the system) obtained by making contour plots of the Hamiltonian with several different values for the constant *c*. The parameters for this figure are: $\Gamma = -10$, $U = 1$, $d = 1.3$ and $s = 1$. From the analysis of this phase portrait one can immediately visualize four fixed points of the system (black dots in the figure): two saddle points (one above and another below the cylinder) and two centers (upstream and downstream of the cylinder). The fixed point upstream of the cylinder is related to the experimental configuration observed in [1]. Therefore, the point vortex model can explain the existence of this unusual stationary vortex configuration in front of the cylinder. The phase portrait on Figure 3 also shows many of the expected characteristics for this system. For example, a vortex placed far above the cylinder will follow an almost straight trajectory to the right, because of the velocity induced by the uniform stream. Similarly, a vortex placed very close to the cylinder (or to the plane) tends to circle around the cylinder (or move parallel to the plane) as expected.

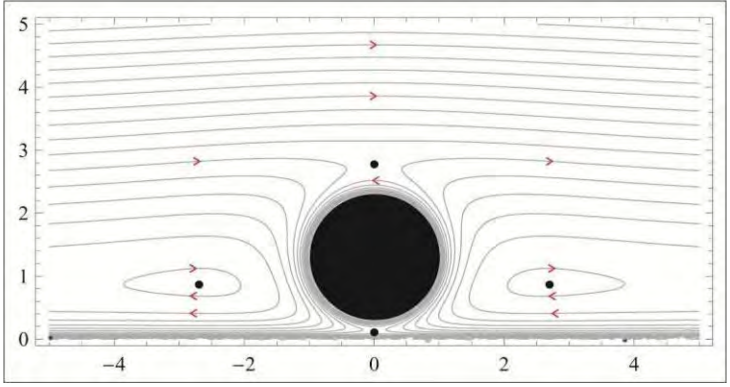

Figure 3
Vortex trajectories obtained by making contour plots of the Hamiltonian. The black dots denote the fixed points and the arrows indicate the motion direction.

Acknowledgements
This work was supported in part by the Brazilian agencies CNPq and FACEPE.

References

[1] W. J. Lin, C. Lin, S. C. Hsieh, and S. Dey, *Flow characteristics around a circular cylinder placed horizontally above a plane boundary*, J. Eng. Mech., 135, 697–716 (2009)
[2] L. Foppl, *Wirbelbewegung hinter einem kreiszylinder*, Sitzb. Bayer. Akad. Wiss., 1, 1–17 (1913).
[3] D. G. Crowdy and J. S. Marshall, *Analytical formulae for the Kirchhoff-Routh path function in multiply connected domains*, Proc. Roy. Soc. A, 461, 2477–2501 (2005)
[4] S. Tang and N. Aubry, *On the symmetry breaking instability leading to vortex shedding*, Phys. Fluids, 9, 2550–2561 (1997)
[5] G. L. Vasconcelos, M. N. Moura, and A. M. J. Schakel, *Vortex motion around a circular cylinder*, Phys. Fluids, 23, 123601 (2011)
[6] P. G. Saffman, *Vortex Dynamics*. Cambridge University Press (1992)
[7] T. W. G. de Laat and R. Coene, *Unsteady force on slender aircraft with free vortices in inviscid flow*, AIAA J., 40, 610–618 (2002)
[8] D. G. Crowdy, *A new calculus for two-dimensional vortex dynamics*, Theor. Comput. Fluid Dyn., 24, 9–24 (2010)
[9] M. N. Moura, *Vortex motion around a circular cylinder both in an unbounded domain and near a plane boundary*, Master's thesis, Federal University of Pernambuco (2012)
[10] C. C. Lin, *On the motion of vortices in two dimensions II: some further investigations on the Kirchhoff-Routh function*, Proc. Natl. Acad. Sci., 27, 575–577 (1941)

Stochastic Dynamical Model of Intermittency with Two Scales

Domingos S. P. Salazar[1] and Giovani L. Vasconcelos[2]

[1] Unidade de Educação a Distância e Tecnologia, Universidade Federal Rural de Pernambuco, 52171-900, Recife, PE, Brazil, [2] Laboratório de Física Teórica e Computacional, Departamento de Física, Universidade Federal de Pernambuco, 50670-901, Recife, PE, Brazil.

Contact email: salazar.domingos@gmail.com

A general stochastic dynamical model of intermittency in highly developed turbulence was recently introduced by the authors [1]. Here it is shown that in the case where only two steps in the energy cascade is considered the probability density functions predicted by the model for both the energy dissipation rate and the velocity increments can be written explicitly in terms of known functions.

Turbulence is often pictured as a set of self-similar structures of different sizes, called eddies, in which energy flows from larger to smaller scales. This qualitative feature known as the energy cascade is commonly found in models of turbulence [2]. In his 1941 theory [3], Kolmogorov assumed a constant energy rate between the stages in the energy cascade and obtained a Gaussian distribution for the velocity increments. Later on, as experiments showed heavy tails for the probability density function (PDF) of velocity increments, Kolmogorov's K41 theory had to be modified to account for fluctuations in the energy transfer, a phenomenon usually called intermittency. In his 1962 theory (K62) [4], following earlier work by Obukhov [5], Kolmogorov introduced a lognormal model for intermittency which showed a better agreement with experiments than the K41 theory, although the K62 model has also been criticized [6].

In the context of Lagrangian turbulence, one usually considers fluctuations of the velocity time increments, $\delta_\tau v(t) = v(t+\tau) - v(t)$, of a fluid particle. It is common to model the dynamics of such velocity increments with a Langevin equation:

$$\dot{\delta_\tau} v = -\gamma \delta_\tau v + \kappa \xi(t), \tag{1}$$

where $\xi(t)$ is a white noise. Solving the stationary Fokker-Planck equation for (1) yields a Gaussian distribution with zero mean for the velocity increments. The second momentum $\langle \delta_\tau u^2 \rangle$ is related to the energy transfer rate ϵ in the scale τ of the measurement: $\langle \delta_\tau u^2 \rangle = \epsilon\tau$, which defines the Gaussian distribution uniquely [2]. This picture changes if, in order to model intermittency, one assumes that the energy transfer rate ϵ is itself a slowly fluctuating quantity with a certain probability distribution. In such case, the equilibrium PDF, $P(\delta_\tau v)$, resulting from (1) for the velocity increments will be given by a mixture of Gaussian distributions. More precisely, the marginal distribution for $\delta_\tau v$ is given by

$$P(\delta_\tau v) = \int_0^\infty \frac{1}{\sqrt{2\pi\epsilon\tau}} exp\left[\frac{-\llbracket(\delta\rrbracket_\tau v)^2}{2\epsilon\tau}\right] f(\epsilon) d\epsilon, \tag{2}$$

where $f(\epsilon)$ is the energy flux PDF at the scale of the measurement.

The stochastic dynamical model of intermittency presented in Ref. [1] introduces a system of stochastic differential equations (SDEs) for the energy transfer rate between successive levels in the energy cascade. Here, for simplicity, we consider a version of this model with only two scales:

$$\dot{\epsilon_2} = -\gamma_2(\epsilon_2 - \epsilon_1) + \sigma_2\epsilon_2\xi_2(t), \tag{3}$$

$$\dot{\epsilon_1} = -\gamma_1(\epsilon_1 - \epsilon_0) + \sigma_1\epsilon_1\xi_1(t), \tag{4}$$

where ϵ_i is the rate of energy (per unit of mass) transferred to eddies with turnover time $\tau = {}^{T_L}\!/_{b^i}$ from larger eddies with turnover time ${}^{T_L}\!/_{b^{i+1}}$, with T_L being is the integral time scale, which is related to the largest eddy turnover time, and $b > 1$. The quantity ϵ_0 is the injected energy rate assumed constant. The parameters γ_i and k_i are constant and $\xi_i(t)$ are mutually independent white noises. This system has interesting properties, namely: (i) the energy transfer rate is always positive $\epsilon_i > 0$; (ii) it is scale invariant in the sense the dynamics is invariant under the change $\epsilon_i \to \lambda\epsilon_i$; (iii) all scales have the same average energy flux, $\langle\epsilon_i\rangle = \epsilon_0$. By solving Fokker-Planck equation for (4) in equilibrium, one obtains an inverse Gamma distribution:

$$f(\epsilon_1) = \frac{1}{\epsilon_1\Gamma(\alpha_1+1)}\left(\frac{\alpha_1\epsilon_0}{\epsilon_1}\right)^{\alpha_1+1} exp\left(-\frac{\alpha_1\epsilon_0}{\epsilon_1}\right), \tag{5}$$

where $\alpha_1 = {}^{2\gamma_1}\!/_{\sigma_1^2}$. Now we make use of the separation of time scales between the two successive steps of the dynamical hierarchy: $\gamma_2^{-1} \ll \gamma_1^{-1}$. The structures at the smallest scale, $i = 2$, are considered much faster than those at the first scale $i = 1$, therefore the random variable ϵ_2 is assumed to relax to a quasistationary regime for a given value ϵ_1 described by a conditional PDF, $f(\epsilon_2|\epsilon_1)$, of the form

$$f(\epsilon_2|\epsilon_1) = \frac{1}{\epsilon_2\Gamma(\alpha_2+1)}\left(\frac{\alpha_2\epsilon_1}{\epsilon_2}\right)^{\alpha_2+1} exp\left(-\frac{\alpha_2\epsilon_1}{\epsilon_2}\right), \tag{6}$$

where $\alpha_2 = {}^{2\gamma_2}\!/_{\sigma_2^2}$. The marginal distribution for ϵ_2 is then written as

$$f(\epsilon_2) = \int_0^\infty f(\epsilon_2|\epsilon_1)d\epsilon_1 . \tag{7}$$

The moments of the distribution of the velocity increments can be found directly from equation (2) for any positive integer p:

$$\langle(\delta_\tau u)^{2p}\rangle = (2p-1)!!\int_0^\infty \epsilon_2^{\frac{p}{2}}\tau^p f(\epsilon_2)d\epsilon_2 . \tag{8}$$

Expression (8) holds if the last term converges.
Now we show that the two scales case yields known distribution for the energy flux and velocity increments. Inserting (5) and (6) into (7) one obtains

$$f(\epsilon_2) = \frac{2}{\epsilon_2}\left(\frac{\alpha_1\alpha_2\epsilon_0}{\epsilon_2}\right)^{\frac{\alpha_1+\alpha_2}{2}} \frac{1}{\Gamma(\alpha_1)\Gamma(\alpha_2)} K_{\alpha_2-\alpha_1}\left(2\sqrt{\frac{\alpha_1\alpha_2\epsilon_0}{\epsilon_2}}\right), \qquad (9)$$

where K is the Bessel's function of second kind. The PDF (9) is an inverse of the K-distribution which has applications, for instance, to radar imagery [7]. The distribution is depicted in Fig. 1, in comparison with the log-normal distribution, where one can notice a slower decay in the tail of $f(\epsilon_2)$

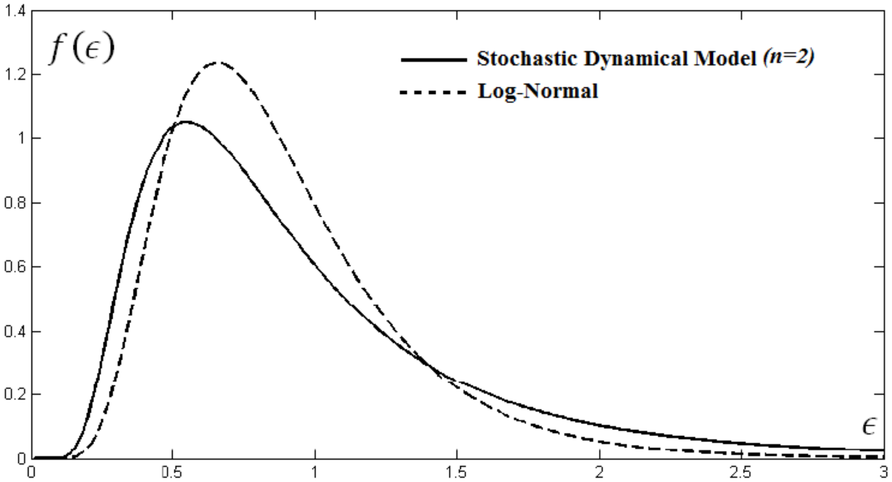

Figure 1
PDF $f(\epsilon_2)$ *for the energy transfer rate in the model with two scales and parameters* $\alpha_1 = \alpha_2 = 5$, $\epsilon_0 = 1$ *and log-normal distribution with same mean and variance.*

The PDF P_2 for velocity increments can be obtained by inserting equation (9) into (2) which results in

$$P_2(\delta_\tau u) = C\left[\frac{[\![(\delta]\!]_\tau u)^2}{2\beta_2\beta_1\epsilon_0\tau}\right]^{-\alpha_2-{}^3/_2} \cdot U\left(\frac{3}{2}+\alpha_2; 1+\beta_2-\beta_1; \frac{2\beta_2\beta_1\epsilon_0\tau}{[\![(\delta]\!]_\tau u)^2}\right), \qquad \mathbf{(10)}$$

where U is the confluent hypergeometric function of second kind and C is a normalization constant given by

$$C = \frac{1}{\sqrt{2\pi}} \frac{\Gamma(\alpha_1 + {}^3/_2)}{\sqrt{\alpha_1}\Gamma(\alpha_1+1)} \frac{\Gamma(\alpha_2 + {}^3/_2)}{\sqrt{\alpha_2}\Gamma(\alpha_2+1)}. \qquad (11)$$

In Fig. 2 we show in a log-linear plot the distribution (10) in comparison with the normal distribution, where the power law behavior in the tails is evident. Inserting equation (9) into (8) one obtains the moments of the distribution $P_2(\delta_\tau u)$:

$$\langle(\delta_\tau u)^{2p}\rangle = (2p-1)!!\,\epsilon_0^p\tau^p \prod_{j=0}^{p-1} \frac{\alpha_1}{\alpha_1 - j}\frac{\alpha_2}{\alpha_2 - j}. \qquad (12)$$

One thus sees a divergence in the moments for $p \geq \alpha_i + 1$, which is another indication that P_2 has a power-law tail. From equation (10), in the limit $\delta_\tau u \to \infty$ one can show that,

$$P_2(\delta_\tau u) \sim a[\![(\delta]\!]_\tau u)^{-2\cdot\alpha'-3}, \qquad \textbf{(13)}$$

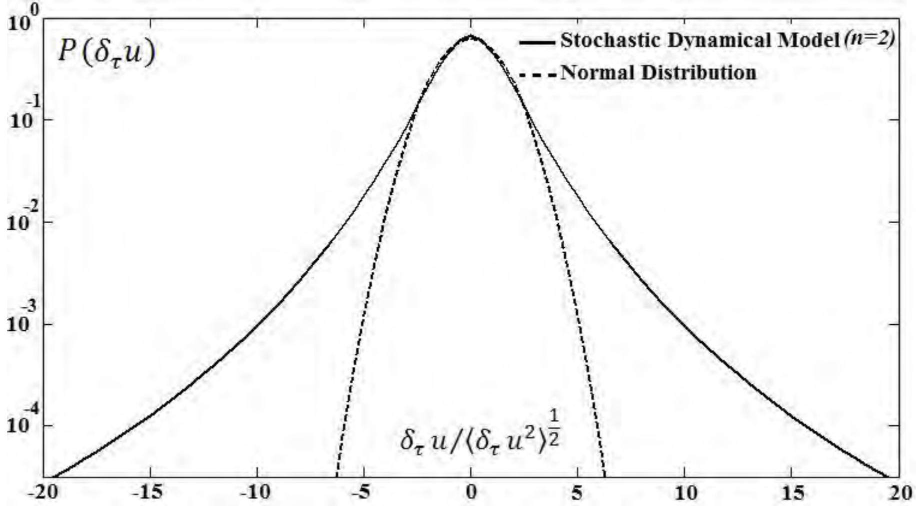

Figure 2
PDF $P_2(\delta_\tau u)$ *for the normalized velocity increments in the model with two scales and parameters* $\alpha_1 = \alpha_2 = 5$ *,* $\epsilon_0 = 1$ *and normal distribution with same mean and variance.*

where a is a positive constant and $\alpha' = \min(\alpha_1, \alpha_2)$.
It was shown in Ref. [1] that the distributions given by (2) for the general case of an arbitrary (finite) number of scales are members of a large class of power-law distributions expressed in terms of generalized hypergeometric (GHG) functions $_nF_0$. In particular, it was noticed that the case $n = 1$ yields a q-Gaussian distribution. Here we have shown that the GHG distribution of second order ($n = 2$) can also be written in terms of more simple functions, namely, the confluent hypergeometric functions.The extension of the above intermittent model to statistical equilibrium of multiscale systems has recently been proposed and its comparison with experimental data from Lagrangian turbulence was also discussed [8]. Applications to other complex systems with multiple spatial or temporal scales are currently under investigation.

Acknowledgements

This work was supported in part by the Brazilian agencies CNPq and FACEPE.

References

[1] D. S. P. Salazar and G. L. Vasconcelos, Phys. Rev. E 82,047301 (2010)
[2] U. Frisch, *Turbulence: The Legacy of A. N. Kolmogorov* (Cambridge University Press, Cambridge, England, 1995)
[3] A. N. Kolmogorov, Dokl. Akad. Nauk SSSR 30, 299 (1941)
[4] A. N. Kolmogorov, J. Fluid Mech. 13, 82 (1962)
[5] A. M. Obukhov, J. Fluid Mech. 13, 77 (1962)
[6] E. A. Novikov, Appl. Math. Mech. 35, 231 (1971)
[7] Jakeman, E. , Journal of Physics A: Mathematics and General, 13, 31–48 (1980)
[8] D. S. P. Salazar and G. L. Vasconcelos, Submitted. (2012)

Micro- and nanoparticle pattern formation in fluids induced by external fields

Arne T. Skjeltorp[1,3], Geir Helgesen[1,2,3]; and Matti Knaapila[1]

[1]Institute for Energy Technology, Kjeller, Norway, [2]Department of Physics, University of Oslo, Norway, [3] 2011-12: The Centre for Advanced Study (CAS) at the Norwegian Academy of Science and Letters, Oslo, Norway

Contact email: arne.skjeltorp@ife.no

Electric and magnetic fields can be used to create nano-and microparticle structures within fluids such as water, oil, ferrofluids or polymers. The particle pattern formations in the fluids are highly dependent on the time and space variations of the external fields. A short review will be given of the pattern formation for various types of particles such as carbon nanoparticle, colloidal microspheres and viruses.

Aligned carbon nanocones in free-standing UV-curable polymer composite

There are fundamental restrictions in the ability to form uniform mixtures of rigid anisotropic particles and flexible polymers, which may not be possible except at the low particle fraction limit [1]. The control of polymer dispersion formation is therefore troublesome for carbon nanotubes (CNTs) [2] considered to be ultimate ‘‘rigid rod polymers’’ [3]. If one could overcome this fundamental problem, it might have far-reaching practical impact. For example many electrostatic discharge (ESD) materials contain rigid carbon particles in a polymer matrix, including carbon fibers and CNT in thermoset polymers like epoxies.

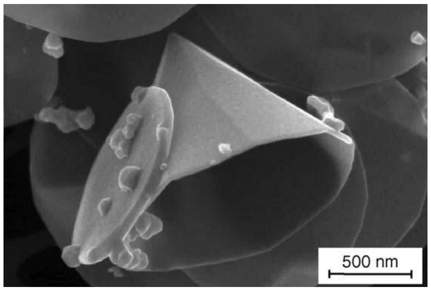

Figure 1
A scanning electron micrograph of carbon nanocone particles (CNC) material.

In the present work [4-6] alternating electric field has been used to assemble and align carbon nanocone particles (CNCs), Fig. 1, into microscopic wires in self-supporting polymer film, Fig. 2. The particle fraction is kept low (one-tenth of the percolation threshold of isotropic mixture), which allows uniform dispersion and efficient UV curing. The alignment leads to the conductivity enhancement of three to four orders of magnitude (from 10^{-7} to 10^{-3} S/m) in the alignment direction. It does not require passing current so the material can be isolated from the alignment electrodes. This prevents electrodes attaching to the film, if the film is adhesive in nature. The alignment can be done using either in-plane or out-of-plane geometries. It is proposed that this concept could be applied in areas such as electrostatic discharge applications where inexpensive conductive or dissipative materials and macroscopic uniformity are prerequisites.

Magnetic field manipulation and self-assembly of nonmagnetic particles in magnetic fluids

A particularly interesting method to self-assemble nano - to millimeter - sized components is the use of the “magnetic hole” effect [7], a “magnetic analogue” of Archimedes’ principle. In this method, nonmagnetic particles can be manipulated by external magnetic fields by immersing them in a dispersion of colloidal, magnetic nanoparticles, denoted ferrofluids. Nonmagnetic particles in magnetized ferrofluids are in many ways ideal model systems to test various forms of particle self-assembly and dynamics.

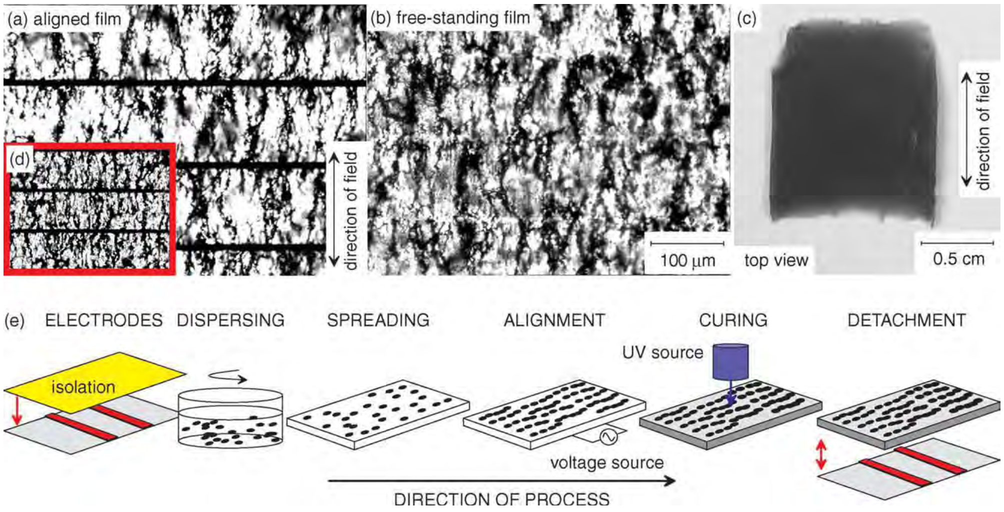

Figure 2
Optical micrographs of thermally cured CNC film (0.2 vol %) processed via in-plane route. (a) Aligned and thermally cured film. The black lines are the alignment electrodes. (b) Aligned free-standing film. (c) A low-magnification photo of the sample shown in (b). Inset (d) shows a corresponding UV-cured film (0.4 vol %). (e) Schematic illustration of the process steps.

When microspheres are confined to a monolayer between two plane parallel planes and subjected to ac magnetic fields, they show a variety of dynamical behaviors and assemblages. We have derived analytical results for the particle pattern formation from the pair-wise competing interactions between the particles and this compare favorably with experimental results, see e.g. refs. [8-9]. In particular, it has been possible to use symbolic dynamics for the analysis of the particle dynamics, Fig.3, and ref. [10].

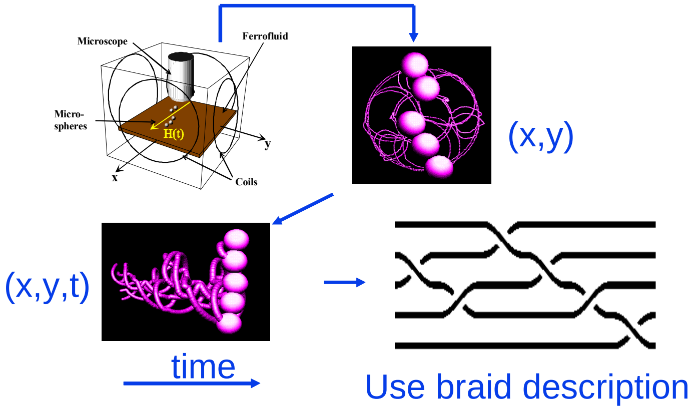

Figure 3
Experimental observation of the trajectories of five magnetic holes subjected to a magnetic field rotating in the (x, y)-plane forming knotted curves. When these trajectories are plotted vs. time these "world lines" can be analysed using notions from braid theory.

When the nonmagnetic particle is reduced from micrometer size to nanometer size and its volume becomes comparable to the mean volume occupied by a ferrofluid (FF) particle, it is a dynamic "magnetic hole" effect forming ordered structures. Some pioneering work was done on tobacco mosaic virus (TMV) [11], which is a hollow cylindrical assembly of length 300 nm and diameter 18 nm. Distinct alignment of the TMV in the ferrofluid has been observed using Small Angle Neutron Scattering (SANS), see Fig. 6.

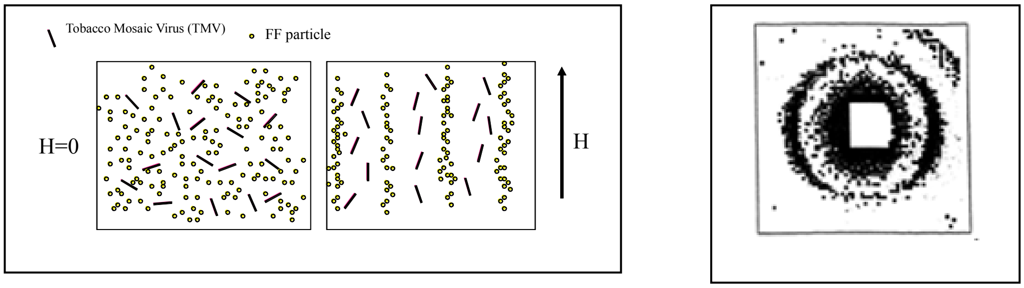

Figure 4
Schematic illustration of the alignment of TMV in a ferrofluid using an external magnetic field, left, and SANS spectrum, right.

To explain this unexpected behaviour, it is necessary to understand the correlations which may develop in a mixed fluid in which two species of particles coexist. The scattering of a mixture of nonmagnetic particles and magnetic particles subjected to a magnetic field can thus be modelled to involve three correlation terms: between the magnetic-and nonmagnetic particles; between the nonmagnetic particles; and between the magnetic particles. The results show that, for typical densities and dipole strengths, the pair probability distributions of each individual type of particle are relatively unperturbed by the presence of the other species. This means that the ferrofluid particles form chains, much as if the non-magnetic particles are not present, while the latter find sufficient room between the chains to act as if the ferrofluid is not present. Due to this type of coexistence, very strong cross-correlations between different types of particles can develop in the system. This means that a ferrofluid particle can expect to have another ferrofluid particle as a neighbour in the direction of the field, but most likely a non-magnetic particle as a neighbour perpendicular to the field, because that is where it has to fit into the dispersion.

References

[1] A. Yu Grosberg and A. R. Khokhlov, Statistical Physics of Macromolecules; American Institute of Physics: Woodbury, NY, 1994.

[2] B. P. Grady, Macromol. Rapid Commun. 31, 247–257 (2010)

[3] M. Moniruzzaman, K. I Winey, Macromolecules 39, 5194–5205 (2006)

[4] Eldrid Svåasand, Geir Helgesen; and Arne T. Skjeltorp, Colloids and Surfaces A: Physicochem. Eng. Aspects 308, 67–70 (2007)

[5] Matti Knaapila et al., J. of Polymer Science: Part B: Polymer Physics, 49, 399–403 (2011)

[6] Matti Knaapila, Jean Patrick Pinheiro, Mark Buchanan, Arne T. Skjeltorp; and Geir Helgesen, Carbon 49, 3171 – 3178 (2011)

[7] A.T. Skjeltorp, Phys. Rev. Lett. 51, 2306–2309 (1983)

[8] R. Toussaint, J. Akselvoll, E.G. Flekkøy, G. Helgesen and A.T. Skjeltorp, Phys. Rev. E 69, 011407 (2004)

[9] G. Helgesen, E. Svåsand; and A.T. Skjeltorp, J. Phys.: Condensed Matter, 20, 204127 (2008)

[10] K. de Lange Kristiansen, G. Helgesen; and A. T. Skjeltorp, Eur. Phys. J. B 51, 363 (2006)

[11] J.B. Hayter, R. Pynn, S.W. Charles, A.T. Skjeltorp, J. Trewhella, G. Stubbs; and P. Timmins, Phys. Rev. Lett., 62, 1667-70 (1989)

An efficient formalism for numerical simulations of dendritic flux avalanches in superconducting films

Jørn Inge Vestgården[1], Daniil Shantsev[1], Yuri Galperin[1, 2], Tom Henning Johansen[1, 2]

[1]Department of Physics, University of Oslo, [2]Centre for Advanced Study at The Norwegian Academy of Science and Letters

Contact email: jornv@fys.uio.no

Dendritic flux avalanches are fascinating phenomenona appearing quite frequently in superconducting films. We show that the dynamical behavior of the avalanches can be very well described by numerical simulations using a continuum approximation of the vortex matter.

When type II superconductors get exposed to applied magnetic field they are unable to shield it completely, and they must permit magnetic flux entering in form of vortices, each carrying one quantum of magnetic flux, *e/2h*. The penetration of vortices is on average rather smooth and slow since the vortices get pinned by the nanometer-sized material defects, and the vortex matter thus forms what is called the critical state, where current density has the value of the critical current density j_c [1].

Occasionally, the critical state can turn unstable when large amounts of magnetic flux rushes in from a seemingly random position at the edge and flows into the interior of the superconductor, where it forms large branching structures. Such events are called dendritic flux avalanches and they have been experimentally observed in many materials, e.g., with magneto-optical imaging [2,3].

The origin of the avalanches is a thermomagnetic instability, where an initial, small increase in temperature yields reduced j_c, which forces magnetic flux into the sample. The moving magnetic flux means dissipation, so the temperature increases even more. Consequently, there is a positive feedback loop, giving rapidly increasing temperature and runaway magnetic flux. Linear stability analysis based on a continuum approximation of the thermomagnetic instabilities have explained many of the experimentally observed threshold for onset of instability [4,5].

The success of the linear stability analysis encourages to see if more results can be drawn from the full, nonlinear theory. In particular, a simulation of the evolution of dendritic patterns is useful, since the process typically last less than 100 nanoseconds, and this time resolution is beyond the reach of most experimental methods. To perform such simulations there are many technical obstacles that must be overcome, where in particular the most challenging is the severe nonlinearity as well as the electrodynamical nonlocality. However, with careful treatment, the model gives a very accurate description of the full process, and in particular it handles dynamically the transition from the slow flux penetration between avalanches to the many orders of magnitude faster instability regime [6]. As an indication of the correctness of the model and the solution, the simulated complex dendritic flux patterns appear almost identical to those seen in experiments.

Figure 1 shows the magnetic flux distribution in a square film obtained by numerical simulation. In three of the sides only the critical state is seen, where the flux penetration is deepest in the center of the sides and shortest in the corners. At the bottom the critical state is disturbed by the presence of the large branching structure. The main trunk extends from the edge to the flux front and just outside the flux front, many branches appear, extending all the way to the sample center.

The simulation shows that dynamical process that leads to the formation of the branching structure has extreme characteristics. First, the whole avalanche is fast and is over in less than 100 nanoseconds. Second, this yields flux propagation velocities as high as 100 km/s. Third, the electric field rises more than five orders of magnitude compared to the value before the avalanche. Fourth, the temperature reaches above the critical value in the dendrite core, i.e., during the avalanche parts of the sample are no longer superconducting.

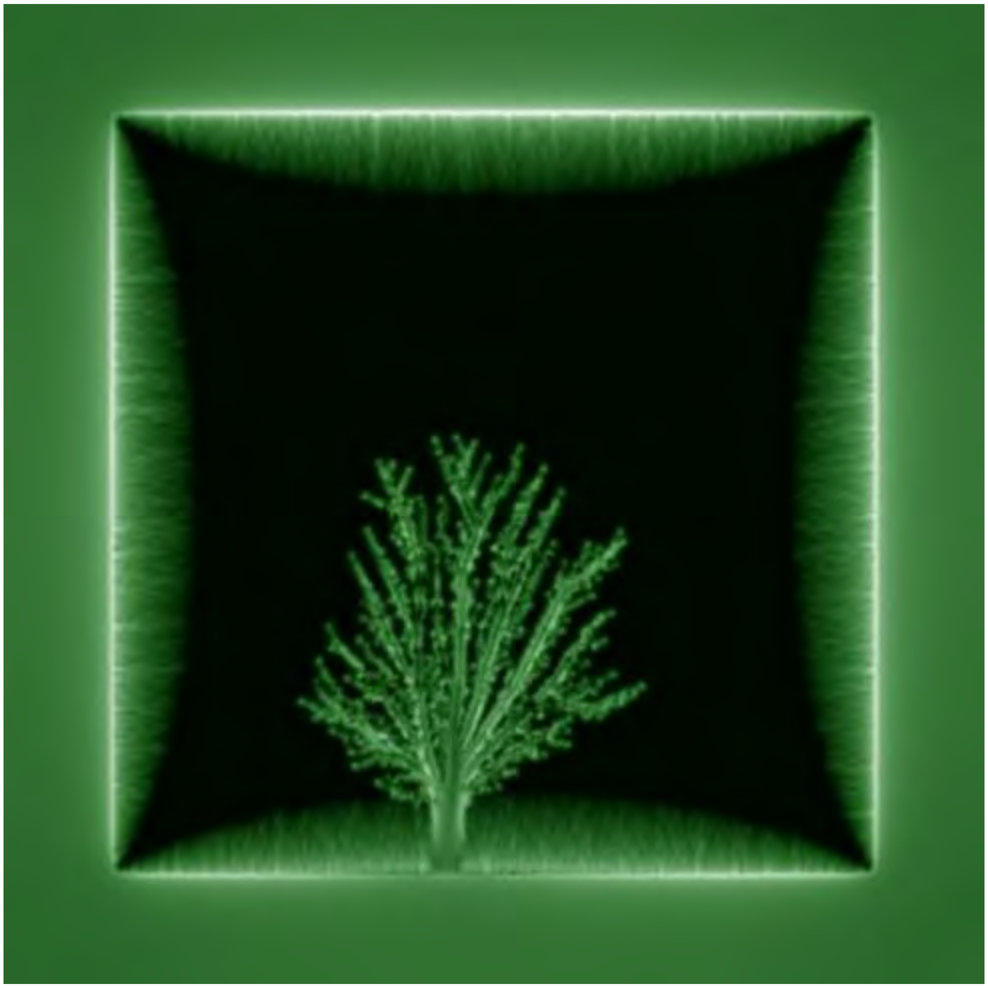

Figure 1
The simulated magnetic flux distribution in a superconducting square with one dendritic flux avalanche. The intensity represents the magnetic flux density B_z, and one can see, as typical for films, that the highest values are at the edges, while the central portion is black, i.e., it is flux-free.

A particularly interesting question is why the instability does not form a fingering structure or a uniform instability front, but instead forms a branching structure? The simulation does not yet answer this question completely, but it gives some clues for the answer. First, there seems to be a characteristic width so that if the branches are too wide they will split. (This does not apply to the trunk, which can be arbitrarily wide.) Second, material disorder is important for the dynamics of the avalanche but it is not the primary mechanism for branching. Third, the branching should be associated with the electrodynamical nonlocality which could play a role analogous to surface tension in viscous fingering. Finally, branching happens in a least three different ways: by symmetric bifurcations, by new branch appearing transverse to a main branch, and by the appearance of multiple branches from the main trunk.

In summary, we show that numerical simulations can give the full flux dynamics of superconducting films, converting both the smooth flux penetration, which builds the critical state, as well as the thermomagnetic instabilities, which result in dendritic flux avalanches.

Acknowledgements

This work was supported financially by the Research Council of Norway (NFR) and Centre for Advanced Study at the Study at The Norwegian Academy of Science and Letters (CAS).

References

[1] E. H. Brandt, *Electric field in superconductors with rectangular cross section*, Phys. Rev. B, 52, 15442 (1995)

[2] E. Altshuler, T. H. Johansen, *Colloquium: Experiments in vortex avalanches*, Rev. Mod. Phys. 76, 471 (2004)

[3] C. A. Durán, P. L. Gammel, R. E. Miller, and D. J. Bishop, *Observation og magnetic-field penetration via dendritic growth in superconducting niobium films,* Phys. Rev. B 52, 75 (1995)

[4] A. L. Rakhmanov, D. V. Shantsev, Y. M. Galperin, and T. H. Johansen, *Finger pattern produced by thermomagnetic instability in superconductors*, Phys. Rev. B 70, 224502 (2004)

[5] D. V. Denisov, D. V. Shantsev, Y. M. Galperin, Eun-Mi Choi, Hyun-Sook Lee, Sung-Ik Lee, A. V. Bobyl, P. E. Goa, Å. A. F. Olsen, and T. H. Johansen, *Onset of Dendritic Flux Avalanches in Superconducting films*, Phys. Rev. Lett. 97, 077002 (2006)

[6] J. I. Vestgården, D. V. Shantsev, Y. M. Galperin, and T. H. Johansen, *Dynamics and morphology of dendritic flux avalanches in superconducting films*, Phys. Rev. B 84, 054537 (2011)

CO_2 and porous media - SANS

Pawel A. Sobas[1], Kenneth D. Knudsen[1,3], Geir Helgesen[1,3], Arne Skjeltorp[1,3], Jon Otto Fossum[2,3]

[1] Physics Department, Institute for Energy Technology, 2027 Kjeller, Norway, [2] Department of Physics, Norwegian University of Science and Technology, Trondheim, Norway, [3]2011-12: Centre for Advanced Study at The Norwegian Academy of Science and Letters, Oslo, Norway

Contact email: pawel.sobas@ife.no

Using small angle neutron scattering and dynamic light scattering we investigate the behaviour of porous materials that were filled with CO_2 in the supercritical and liquid states. These techniques, which are slightly modified in order to be used with a specialized pressure-temperature cell, help us to understand the fluid solid interactions in confined systems.

We are presently involved in research activities focusing on physical processes that are important for the understanding of CO_2 transport and storage into the ground. CO_2 transport into geological structures can be done on-shore or off-shore. The relevant geological formations may show large variations in composition (water saturated porous materials, such as sandstone in a sedimentary basin, caprock, clays). CO_2 trapped in such porous materials relies on different mechanisms of confinement [1] that act on different time scales. Physical trapping of CO_2 may take as much as 100 years. The next stage, solubility in water, can last for 1000 years or more. The final stage is mineralization, which may take up to 10000 years. Taking this into account, some important factors to consider are: 1) an impermeable caprock that keeps the fluid underground (supercritical CO_2 fluid), 2) the solubility of the CO_2 in the water, 3) intercalation (absorption) into clay nanopores, 4) chemical reactions that bind the carbon in mineral form to the rock.

Small Angle Neutron Scattering (SANS) is a technique highly valuable for studying nanostructures (1-100 nm), such as clays nanoparticles, and this technique is available at Institute for Energy Technology (IFE). For the investigations of CO_2 and porous materials we will employ a specially designed cell to be used in combination with SANS. The cell allows studying nanoporous materials together with CO_2 in the supercritical state, up to 150°C and CO_2 pressure up to 690 bars. A specially adapted setup has now been made in order to integrate this CO_2 cell into the SANS apparatus. In addition, the instrument has been upgraded by the implementation of a novel element - a so-called bender. This is designed to deflect neutrons with wavelengths above 4.5 Å by a certain amount (4°), over a short distance (cm), thus removing fast neutrons and gamma radiation, in order to improve the quality of the neutron beam. The bender consists of a set of wafers coated on the outer side of the channels with Ni-Ti supermirrors with reflectivity ratio $m = 2.5$ and on the inner side with 1.5µm of Gd to transmit a reduced divergence.

Integration of the CO_2 cell into the SANS machine will help us to answer some relevant and fundamental problems like:

- understanding of the behaviour of CO_2 in materials with significant nano-porosity (e.g. clay / caprocks),
- wetting and adsorption for varying nanopore sizes and geometries (cylindrical / slit),
- dynamics and flow behaviour of CO_2 in such confined systems,
- modification of the behaviour when CO_2 coexists with water inside the pores.

So far little fundamental research has been done on supercritical CO_2 storage in geological formations. We want to start with model compounds (aerogels, porous glass etc.) for proper understanding, and then look at sorption in specific clay systems. For some pore types the assumption of a uniform filling turns out not to be correct [2], and a high-density CO_2 layer (1.1 g/cm^3) is formed near the pore surface, due to attractive forces and enhanced by nanopore field effects.

We plan to extract information about pore content from the following measurements:

- (scattered intensity)$^{1/2}$ plotted vs. density of CO_2 ρ_{CO2} $\rightarrow$ 2- or 3-phase system,
- transmission measurements → density of adsorbed material,
- scattering invariant → volume fraction of adsorbed phase.

In recent years Dynamic Light Scattering (DLS) has been widely used to characterize the dynamic properties of particles in supercritical fluids (SFCs) [3]. We have started applying the DLS technique for supercritical CO_2 measurements of nanoparticle sized polystyrene (as model particles), clays, and other nanoparticles. For the DLS measurements we used the same CO_2 cell as for SANS but because of the unique design of our cell the DLS technique had to be slightly modified for our purposes. We performed DLS measurements in backscattering mode where the angle between the laser incident beam and the scattered light is in a range of 155° - 175°.
The design of the CO_2 cell is such that it should allow us to use it in other applications like, for example, optical observations of particles (sedimentation) in supercritical and liquid CO_2, H_2O and D_2O, alcohols, as well as mixtures of CO_2 and water.

Acknowledgments

CLIMIT Project 200041, *"Sorption and migration of* CO_2 *in Porous Media"*

References

[1] Melnichenko Y. *et al.*, *Accessibility of pores in coal to methane and cardon dioxide*, Fuel 91, 200-208 (2012)
[2] Melnichenko Y. *et al.*, *Adsorption of supercritical* CO_2 *in aerogels as studied by small-angle neutron scattering and neutron transmission techniques*, J. Chem. Phys. 124, 204711 (2006)
[3] Melnichenko Y., Brown W., Rangelov S., Wignall G.D., Stamm M., *Dynamic and static correlations in solutions of polymers in liquid and supercritical solvents: dynamic light scattering and small angle neutron scattering*, Physisc Letters A 268, 186-184 (2000)

CONTENTS

Sponsors:

Universidade Federal de Pernambuco
DEPARTAMENTO DE FÍSICA

CAS OSLO
complex
www.complexphysics.org
Centre for Advanced Study
at the Norwegian Academy of Science and Letters

The Research Council of Norway

CNPq 60 ANOS

CAPES

FACEPE

PROPESQ
PRÓ-REITORIA PARA ASSUNTOS DE PESQUISA E PÓS-GRADUAÇÃO

complexphysics.org
ISBN 978-82-93224-07-5

Webedition